

JGR Atmospheres



RESEARCH ARTICLE

10.1029/2022JD037942

Key Points:

- We perform nested air quality simulations over the Midwestern US, with the inner domain resolution at a 1.3 km neighborhood-scale
- NO₂ and PM_{2.5} hotspots are simulated adjacent to major roadways, with substantial pollutant differences between urban and rural settings
- Pollutants within Chicago are simulated to have substantial neighborhood-to-neighborhood concentration disparities

Supporting Information:

Supporting Information may be found in the online version of this article.

Correspondence to:

A. Montgomery,
stacy@earth.northwestern.edu

Citation:

Montgomery, A., Schnell, J. L., Adelman, Z., Janssen, M., & Horton, D. E. (2023). Simulation of neighborhood-scale air quality with two-way coupled WRF-CMAQ over southern Lake Michigan-Chicago region. *Journal of Geophysical Research: Atmospheres*, 128, e2022JD037942. <https://doi.org/10.1029/2022JD037942>

Received 30 SEP 2022

Accepted 1 MAR 2023

Author Contributions:

Conceptualization: Anastasia Montgomery, Jordan L. Schnell, Daniel E. Horton

Data curation: Jordan L. Schnell, Zachariah Adelman, Mark Janssen

Formal analysis: Anastasia Montgomery, Jordan L. Schnell

Funding acquisition: Daniel E. Horton

Investigation: Anastasia Montgomery

Methodology: Anastasia Montgomery, Jordan L. Schnell

© 2023. The Authors.

This is an open access article under the terms of the [Creative Commons Attribution-NonCommercial-NoDerivs](#) License, which permits use and distribution in any medium, provided the original work is properly cited, the use is non-commercial and no modifications or adaptations are made.

Simulation of Neighborhood-Scale Air Quality With Two-Way Coupled WRF-CMAQ Over Southern Lake Michigan-Chicago Region

Anastasia Montgomery¹ , Jordan L. Schnell² , Zachariah Adelman³, Mark Janssen³, and Daniel E. Horton^{1,2} 

¹Department of Earth and Planetary Sciences, Northwestern University, Evanston, IL, USA, ²Institute for Sustainability and Energy at Northwestern (ISEN), Northwestern University, Evanston, IL, USA, ³Lake Michigan Air Directors Consortium (LADCO), Rosemont, IL, USA

Abstract The southern Lake Michigan region of the United States, home to Chicago, Milwaukee, and other densely populated Midwestern cities, frequently experiences high pollutant episodes with unevenly distributed exposure and health burdens. Using the two-way coupled Weather Research Forecast and Community Multiscale Air Quality Model (WRF-CMAQ), we investigate criteria pollutants over a southern Lake Michigan domain using 1.3 and 4 km resolution hindcast simulations. We assess WRF-CMAQ's performance using data from the National Climatic Data Center and Environmental Protection Agency Air Quality System. Our 1.3 km simulation slightly improves on the 4 km simulation's meteorological and chemical performance while also resolving key details in areas of high exposure and impact, that is, urban environments. At 1.3 km, we find that most air quality-relevant meteorological components of WRF-CMAQ perform at or above community benchmarks. WRF-CMAQ's chemical performance also largely meets community standards, with substantial nuance depending on the performance metric and component assessed. For example, hourly simulated NO₂ and O₃ are highly correlated with observations ($r > 0.6$) while PM_{2.5} is less so ($r = 0.4$). Similarly, hourly simulated NO₂ and PM_{2.5} have low biases (<10%), whereas O₃ biases are larger (>30%). Simulated spatial pollutant patterns show distinct urban-rural footprints, with urban NO₂ and PM_{2.5} 20%–60% higher than rural, and urban O₃ 6% lower. We use our 1.3 km simulations to resolve high-pollution areas within individual urban neighborhoods and characterize seasonal changes in O₃ regimes across tight spatial gradients. Our findings demonstrate both the benefits and limitations of high-resolution simulations, particularly over urban settings.

Plain Language Summary In this study we use an air quality model to simulate air pollution at very fine spatial scales over a central midwestern U.S. domain that includes Chicago, IL and Milwaukee, WI. We assess our model's performance relative to meteorological and air quality observations and then characterize the spatial patterns of modeled pollutants. We find large differences in air pollution between urban and rural settings. Because our model operates at fine spatial scales, we are also able to discuss differences in air pollution in different neighborhoods in individual cities. In Chicago, we find elevated pollution near highways and in south and west side neighborhoods, findings that are consistent with previous reports of disparate air quality related health impacts.

1. Introduction

Exposure to poor air quality in the U.S. has been found to exacerbate respiratory diseases (Kurt et al., 2016), drive disparate health burdens in racial minority populations (Jbaily et al., 2022; Tessum et al., 2021), and contribute to ~100,000 premature deaths annually (Goodkind et al., 2019). Given the substantial public health burden associated with exposure to poor air quality, it is essential to resolve pollutant concentrations at high spatiotemporal resolutions. Pollutant exposure in high population settings, that is, urban environments, can vary widely, which can contribute to disparities in health outcomes on a neighborhood-by-neighborhood basis across individual cities (Alexeeff et al., 2018; O'Leary & Lemke, 2014; Southerland et al., 2021). Determining the relationship between heterogeneous pollutant exposure and disparate health effects is challenging given observational constraints. For example, regulatory-grade air quality monitoring stations are relatively sparse and therefore spatial coverage is limited, particularly in urban settings. Observing platforms that do have better spatial coverage, for example, remote sensed satellite observations, often have temporal limitations such as making only one observation a day

Resources: Daniel E. Horton
Supervision: Daniel E. Horton
Validation: Anastasia Montgomery
Visualization: Anastasia Montgomery
Writing – original draft: Anastasia Montgomery
Writing – review & editing: Anastasia Montgomery, Jordan L. Schnell, Zachariah Adelman, Mark Janssen, Daniel E. Horton

in the case of polar orbiters (Penn & Holloway, 2020). Given the need to resolve pollutants across impact-relevant scales (Clark et al., 2022), researchers often turn to physics- and chemistry-based Chemical Transport Models (CTMs) which allow for the spatial heterogeneity of pollutants to be estimated at high temporal resolutions in areas that are otherwise unmonitored (J. Hu et al., 2019).

State-of-the-science CTMs resolve pollutants at ever-increasing spatiotemporal scales. For example, the Community Multiscale Air Quality modeling system (CMAQ; Byun & Schere, 2006) was developed by the U.S. Environmental Protection Agency (EPA) to study the complex interactions of pollutants and meteorology and increase our understanding of atmospheric processes. Over time, the spatial resolution of CTMs like CMAQ has increased as computational costs decrease and spatially-defined inputs are resolved at finer scales (Gan et al., 2016). Higher resolution CTM studies have the potential to simulate more accurate meteorology, emissions, and pollutant concentrations than coarser resolution models (Fountoukis et al., 2013; Gan et al., 2016; Torres-Vazquez et al., 2022). However, some simulated meteorological and chemical variables may show lower model performance at finer resolutions because of incomplete characterizations of complex terrain and limitations in the planetary boundary layer formation (Tran et al., 2018; Zhang et al., 2014). Notably, epidemiological studies have identified the use of high-fidelity, high-resolution air quality characterizations as better at capturing pollution-related health impacts (Jiang & Yoo, 2018; Southerland et al., 2021; Thompson et al., 2014).

Given the potential benefits of high resolution CTM studies, here we utilize WRF-CMAQ to characterize pollutant concentrations over a southern Lake Michigan domain, a region in the central midwestern U.S., which includes the major population centers of Chicago, IL and Milwaukee, WI. Previous modeling studies have focused on this region due to the atmospheric complexities associated with Lake Michigan and high O₃ pollution in the region (Abdi-Ouskouei et al., 2020; Dye et al., 1995; Foley et al., 2011). By and large, air quality in this region has been improving due to emission controls and the outsourcing of industry and manufacturing (Jing et al., 2014). However, pockets of poor air quality persist, particularly in and downwind of urban centers like Chicago, which has been in EPA 8-hr O₃ National Ambient Air Quality Standards (NAAQS) non-attainment status since 2004 (EPA, 2022).

From a regional perspective, poor air quality in Midwestern summers is often associated with warm stagnant air masses (Jing et al., 2017; Schnell & Prather, 2017; Tai et al., 2010), while near-surface winter pollution is largely restricted to particulate matter accumulations associated with temperature inversions (Tran et al., 2018). However, at local scales, local geography, meteorology, and emissions often play a synergistic role. For example, in Chicago, the coastal geography, micro-meteorology, and high-emitting urban footprint combine to create an active atmospheric regime that often facilitates accumulation of primary pollutants and/or the precursors of secondary pollutants. Indeed, Chicago's O₃ NAAQS nonattainment status is a direct result of interacting emissions, geography, and meteorology—particularly the interaction of precursor emissions with Lake Michigan's lake breeze. Because the formation of O₃ is generally dependent on the ratio of precursor emissions, that is, nitrogen oxides (NO_x) and volatile organic compounds (VOCs), the EPA has restricted NO_x emissions (EPA, 2018). However, previous studies have found that Chicago is in a transitional or VOC-limited regime (Duncan et al., 2014; Jin et al., 2017; Jing et al., 2014)—suggesting a limitation to the efficacy of emissions controls that only consider NO_x and do not also reduce VOCs.

Similar to O₃, the concentration of NO₂ depends on meteorological factors such as winds and temperature (Harkey et al., 2015), however given the relatively short lifetime of NO₂, proximity to emission sources also plays a substantial role, particularly in the development of intra-urban heterogeneities. In satellite analyses, Chicago appears as a large source of NO₂ pollution to the greater Midwest (Goldberg et al., 2021), a factor that contributes to the formation and elevated concentration of downwind/rural O₃. In addition, NO₂ can be a precursor to PM_{2.5} formation through the oxidation of NO₂ to nitrate. While Chicago is currently in compliance with PM_{2.5} standards, PM_{2.5} has previously been found to be elevated in comparison with rural areas due to the confluence of transportation, energy generation, and industrial emissions, as well as atmospheric transport, and secondary formation processes (Zhang et al., 2014).

Given the above complexities, we hypothesize that the characterization of air quality in the southern Lake Michigan-Chicago region would benefit from resolving fine scale interactions and impacts of local geography on atmospheric chemistry and meteorology. As such, here we use a high-spatial resolution numerical model that includes atmospheric meteorology, chemistry, and components of their interactions and feedbacks, that is, the two way-coupled Weather Research and Forecasting-Community Multiscale Air Quality modeling system

(WRF-CMAQ). These high-resolution simulations are made possible by the Lake Michigan Air Directors Consortium (LADCO) spatial surrogate data set (LADCO, 2022), which defines the allocation of county-level emission information to a 1.3 km grid. We characterize our air quality estimates as “neighborhood-scale,” because our 1.3 km simulations have an average of ~ 5 grid cells for each of the 77 community areas that comprise Chicago (Chicago Data Portal, 2022). LADCO spatial surrogates are used in the Sparse Matrix Operating Kernel of Emissions (SMOKE) processing system (B.H. Baek & Seppanen, 2018) with the U.S. EPA 2016 Beta modeling platform (Eyth et al., 2019) to produce emission data for our 1.3 km grid. We use this emissions data set in WRF-CMAQ to simulate 4 months representative of the four meteorological seasons and characterize pollutant concentrations over a central-Midwestern and Chicago-centric domain.

2. Methods

2.1. CTM Simulations and Domains

We performed CTM simulations using the two-way coupled Community Multi-scale Air Quality (CMAQ, v5.2; Byun & Schere, 2006) and Weather Research and Forecasting (WRF, v3.8; Skamarock et al., 2008) modeling system (WRF-CMAQ; Wong et al., 2012). The two-way configuration of WRF-CMAQ allows feedbacks between simulated aerosols and WRF's shortwave radiation scheme. To perform WRF-CMAQ simulations, we follow the methodology of Wong et al. (2012): (a) we produce dynamically downscaled meteorology with stand-alone WRF simulations, (b) we then use the stand-alone WRF output to create meteorologically-informed emissions data using the Sparse Matrix Operating Kernel of Emissions (SMOKE), and lastly (c) we run the coupled WRF-CMAQ model, incorporating the meteorologically-informed SMOKE emissions data.

To generate boundary and initial conditions and facilitate the production of meteorologically-informed emissions data, we first perform a stand-alone WRF simulations to generate three-dimensional meteorology in nested domains with 12 km (CONUS; d01), 4 km (Midwest; d02), and 1.3 km (southern Lake Michigan; d03) resolutions (Figure 1a). We use a 10-day spin-up period and simulate 4 months—August 2018, October 2018, January 2019, and April 2019—using a 60-, 20-, and 6-s timestep for the 12, 4, and 1.3 km domains respectively. To allow soil moisture and soil temperature variables to reach a state of statistical equilibrium with observational constraints, we turn on the soil moisture initialization option during the 10 days spin-up (Pleim & Xiu, 2003). We run WRF with 35 vertical layers from the surface to 30 hPa with a lowest model level thickness of ~ 20 m. Initial conditions and 3 hourly lateral boundary conditions for the 12 km domain are sourced from the North Atlantic Regional Reanalysis (NARR; Mesinger et al., 2006). Simulated WRF meteorology is nudged toward reanalysis using Four-Dimensional Data Assimilation (FDDA) above the boundary layer, using nudging coefficients from LADCO (2022) and Otte (2008) for temperature and wind (3×10^{-4} , 1×10^{-5} , and $1 \times 10^{-6} \text{ s}^{-1}$ for 12, 4, and 1.3 km) and the water vapor mixing ratio (1×10^{-5} , 1×10^{-6} , and $1 \times 10^{-7} \text{ s}^{-1}$ for 12, 4, and 1.3 km). We incorporate the land cover product from the National Land Cover Database (NLCD; Dewitz, 2021) at a 9 arc-second resolution. For the WRF physics options, we select the Morrison 2-moment microphysics scheme (Morrison et al., 2009), version 2 of the Kain-Fritsch (KF2) cumulus cloud parameterization for the 12- and 4-km simulations (Kain, 2004), the Asymmetric Convective Model version 2 (ACM2) for the planetary boundary layer (Pleim, 2007) and the Pleim-Xiu land surface model (Xiu & Pleim, 2001) with soil moisture and temperature nudging (Pleim & Gilliam, 2009; Pleim & Xiu, 2003). We use the Rapid Radiative Transfer Model for GCMs (RRTMG; Clough et al., 2005) for both our shortwave and longwave radiation schemes.

To create 4 and 1.3 km emissions inputs for use in WRF-CMAQ, we processed the EPA's 2016 Beta emissions modeling platform with the SMOKE software. We process the 2016v7.2 National Emissions Inventory (Eyth et al., 2019) using the 2016 SMOKE Beta Platform, relying on 4 km spatial surrogates provided by CMAS (EPA, 2022) and 1.3 km spatial surrogates provided by LADCO (LADCO, 2022). The spatial surrogates map county-level emissions inventories to model grid cells by using the geographic attributes of the modeling area (such as population, industry, and economic activity). Meteorological conditions are a key factor in determining various vehicle emission processes such as tailpipe exhaust, evaporative processes, brake and tire wear, idling, cold starts (wherein an engine has been at rest for 12+ hrs), and hoteling (wherein long-haul trucks idle for extended rest periods) (SMOKE v4.5 User's Manual, 2017). As such, we integrate the 2018 and 2019 stand-alone WRF-simulated meteorology into the MOVES version developed for the 2016 beta platform, using the 2016 MOVES activity data (Eyth et al., 2019). We use SMOKE to create emissions for the on-road, point, and nonpoint sectors, with meteorology affecting the point, onroad, and some non-point sector processes. We calculate biogenic

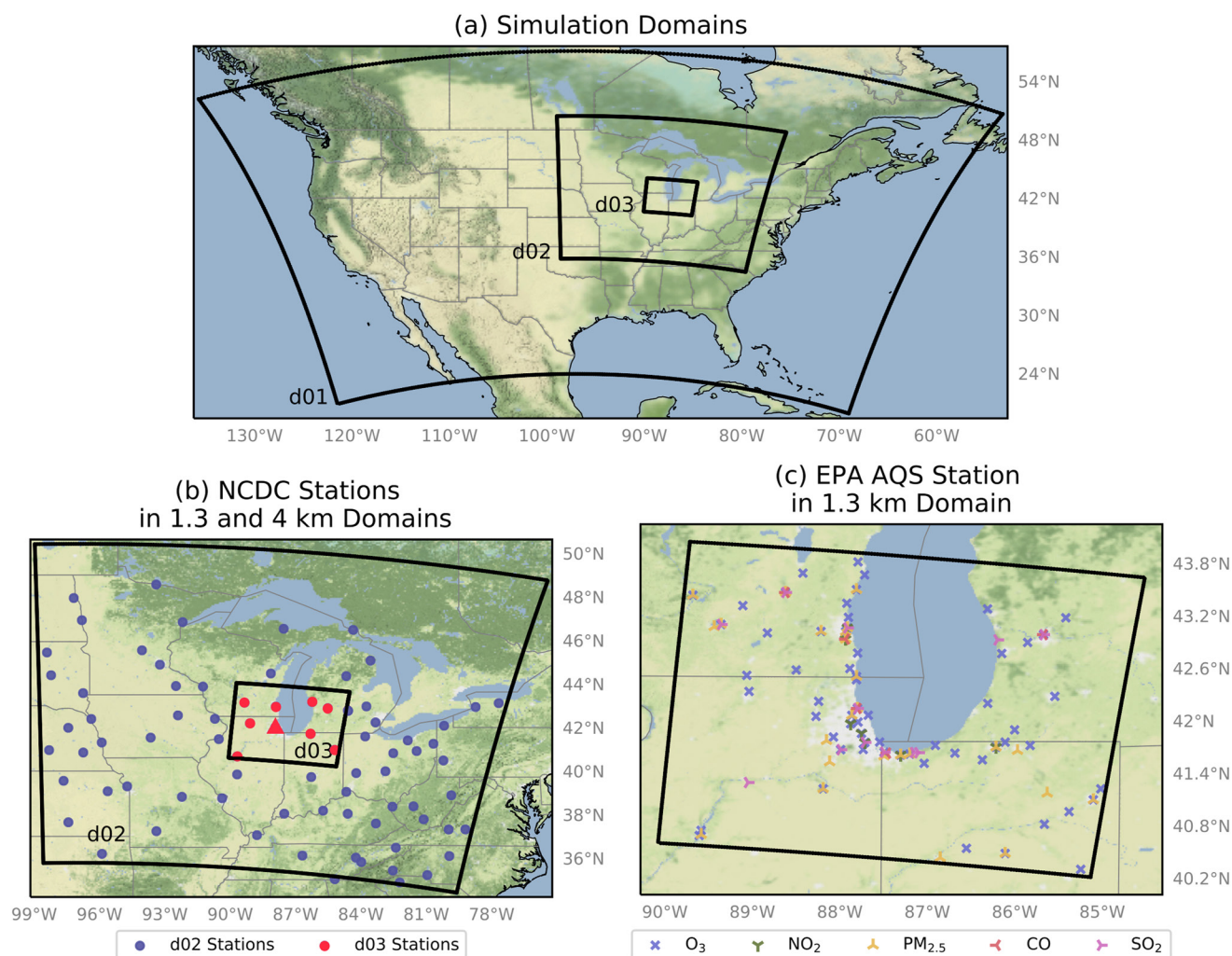


Figure 1. Nested model domains and observation sites. (a) Spatial footprint of nested model domains. We perform stand-alone and Weather Research and Forecasting simulations at 12 km horizontal resolution in the d01 domain. Dynamically downscaled two-way coupled WRF-CMAQ simulations are performed in the d02 and d03 domains at 4 and 1.3 km horizontal resolutions. (b) We use Local Climatological (LCD) Data from the National Climatic Data Center for meteorological validation of the 4 km (d02, purple) and 1.3 km (d03, pink) domains. The station located at Chicago-O'Hare is indicated by a triangle in the center of the d03 domain in panel (b). (c) Environmental Protection Agency Air Quality System (AQS) stations are used to validate simulated pollutants. AQS stations are colored by chemical species and several AQS sensors for different chemical species are co-located, thus overlap on the map.

emissions (BEIS), lightning NO_x emissions, and windblown dust “inline” during the coupled WRF-CMAQ simulation. Within the point sector, we use 2018 and 2019 CEM data to integrate the reported energy-generating unit data.

To ultimately simulate atmospheric pollutants, we run the two-way coupled version of WRF-CMAQ at 4 and 1.3 km. We first run coupled WRF-CMAQ over the 4 km domain using the meteorological boundary conditions from the 12 km stand-alone WRF simulation, nudging from NARR (3-hourly resolution) and chemical boundary and initial conditions from CAM-Chem (Emmons et al., 2020; The CESM2 Development Team, 2019), with chemical variables mapped in Table S1 in Supporting Information S1. We run the coupled 4 km simulation with an 18-s time step and 10-min radiation time step, with CMAQ coupled every eight WRF steps. We then use the 4 km output as meteorological and chemical boundary conditions for the 1.33 km WRF-CMAQ simulation. For the 1.33 km WRF-CMAQ simulation, we run WRF with a 6 s time step and 5-min radiation time step, with CMAQ coupled every eight WRF steps. Both the 4 and 1.3 km simulations integrate the Carbon Bond Mechanism version 6 and aerosol module version 6 with aqueous chemistry (cb6r3_ae6_aq) to create atmospheric constituents. For the two-way WRF-CMAQ 4 and 1.3 km simulations, we applied FDDA coefficients to keep

Table 1
Comparison of Two-Way Coupled WRF-CMAQ Simulated Hourly Meteorological Variables With National Climatic Data Center Observations for 1.3 km (d03) Simulations

Var	Month	μ_d	μ_p	MB	ME	RMSE	r
T2 (°C)	08/2018	23.2	24.0	0.8*	1.8	2.4	0.9
	10/2018	10.8	11.1	0.3	1.8	2.3	0.9
	01/2019	-5.8	-5.0	0.8*	1.9	2.5	1.0
	04/2019	9.2	9.2	0.0	1.9	2.5	0.9
	Average	9.4	9.8	0.5	1.9	2.4	0.9
RH (%)	08/2018	76.6	71.0	-5.7	11.1	14.4	0.7
	10/2018	74.8	76.6	1.9	12.2	15.4	0.7
	01/2019	74.6	78.6	4.0	9.6	11.7	0.7
	04/2019	66.1	71.9	5.8	12.4	16.1	0.8
	Average	73.0	74.5	1.5	11.3	14.4	0.7
WS (m/s)	08/2018	6.9	6.1	-0.7*	2.9	3.7*	0.6
	10/2018	8.8	7.3	-1.5*	3.2	4.1*	0.7
	01/2019	10.2	10.1	-0.1	3.4	4.7*	0.7
	04/2019	10.6	8.3	-2.3*	3.8	4.8*	0.7
	Average	9.1	8.0	6.7	22.3	35.4	0.6
WD (°)	08/2018	166.0	196.7	30.7*	78.8*	127.8	0.3
	10/2018	190.6	207.7	17.1*	53.6*	102.2	0.5
	01/2019	192.8	208.5	15.7*	41.4*	89.5	0.6
	04/2019	166.8	171.0	4.3	52.2*	99.4	0.6
	Average	179.1	196.0	17.0	56.5	104.7	0.5

Note. The average observed value is noted as μ_d , while the predicted value is noted as μ_p . * Indicates performance outside of Emery and Tai (2001) suggested benchmarks (Table S3 in Supporting Information S1).

the model simulation closer to observations above the boundary layer, using default nudging coefficients for temperature and wind ($3 \times 10^{-4} \text{ s}^{-1}$) and the water vapor mixing ratio ($1 \times 10^{-5} \text{ s}^{-1}$).

3. Results

To present our two-way coupled WRF-CMAQ simulations and highlight their ability to resolve neighborhood-scale air quality, we begin with evaluations of the model's domain-wide meteorological and chemical performance across temporal scales. We then highlight the utility of simulations that resolve air quality within individual neighborhoods by conducting an in-depth analysis of intra-urban air quality by characterizing pollutant heterogeneities across Chicago, IL and their interactions with local meteorological features, infrastructure, emissions sources, and the temporal distribution of emissions. Lastly, we assess the benefits, and in some cases disbenefits, of higher spatial resolution for model-observation fidelity performance.

We begin by comparing model-simulated air quality and meteorological data from our highest resolution 1.3 km domain (d03; Figure 1) to ground-based observations. We evaluate model performance for each simulated month. Our air quality performance evaluation primarily focuses on O_3 , NO_2 , and $\text{PM}_{2.5}$, although other EPA criteria pollutants (i.e., CO and SO_2) are also discussed. We evaluate model fidelity to meteorological and air pollutant observations using the following performance metrics: mean observation (μ_d), mean prediction (μ_p), normalized mean bias (NMB), normalized mean error (NME), correlation coefficients (r), mean error (ME), mean bias (MB), and root mean squared error (RMSE) as defined in Table S2 in Supporting Information S1. By normalizing model-simulated variables, the statistical performance of our simulations can be compared to similar model simulations performed over locations with different meteorology, emission profiles, and chemical regimes.

3.1. WRF-CMAQ Meteorological Performance

To assess the performance of the two-way coupled WRF-CMAQ meteorological output over the 1.3 km domain, we compare model simulated variables to ground-based measurements of meteorological conditions. We use hourly observational data from METAR stations aggregated by the National Climatic Data Center (NCDC) (Figure 1b). We focus on 2-m temperature (T2) and relative humidity (RH) at 2 m, and wind speed (WS) and wind direction (WD) at 10 m, each of which is important to the fate and transport of atmospheric pollutants. We evaluated model fidelity using the performance recommendations outlined in Table S3 in Supporting Information S1 (Emery & Tai, 2001). Model-observation comparisons occur where WRF grid cells contain NCDC stations (Figure 1b). The 1.3 km domain contains 10 NCDC stations, which allows for model-observation comparison and assessment at 0.01% of the simulation grid cells (90,720 total). We also assess the model's meteorological performance within Chicago city limits, which has a single NCDC station.

In Table 1, we summarize the model's 1.3 km domain (d03) hourly meteorological performance against observations. We assess diurnal meteorological performance in Figure S1 in Supporting Information S1. For each month, WRF-CMAQ simulated T2, WD, and WS meet the correlation performance criteria suggested by Emery and Tai (2001) (Table S3 in Supporting Information S1). Emery and Tai (2001) do not make RH performance recommendations. WRF performance is best when simulating T2; model-station agreements have low biases and errors, though January 2019 and August 2018 have slightly higher biases than Emery and Tai's (2001) suggested benchmark (Table 1). Model simulations have a consistent warm bias across seasons, with the highest biases in August 2018 and January 2019 ($MB = 0.8^\circ\text{C}$), and highest mean errors in January 2019 and April 2019 ($ME = 1.9^\circ\text{C}$). Simulated RH is also highly correlated with observations ($r > 0.70$), with the highest bias and

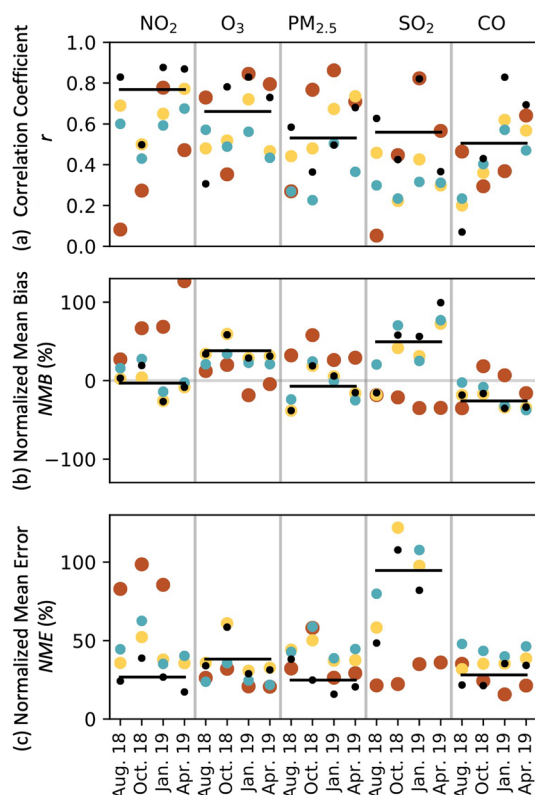


Figure 2. Model performance relative to observations of 5 pollutants over 5 different time-averaging periods: hourly (red), daily (yellow), daily maximum (blue), and monthly (black). The average of the four simulation months, each drawn from a different meteorological quarter, that is, the annualized performance is depicted as a black horizontal line. Each panel summarizes a key performance metric: (a) correlation coefficient (Pearson r), (b) normalized mean bias (NMB), (c) and normalized mean error (NME).

our simulation period, there were a maximum of 10 NO_2 , 67 O_3 , 29 $PM_{2.5}$, 8 SO_2 , and 5 CO monitors, though some stations occasionally drop offline during our simulation period. Notably, the number of O_3 monitors drops from 67 to 23 in January 2019. We filter EPA station data by removing observations with negative concentration values and quality assurance flags.

We compare model simulated pollutants to AQS observations over several different time scales, including 4-monthly or annualized mean, monthly mean, daily mean, hourly mean, and daily maximum (Figure 2). We calculate the annualized mean by averaging across our simulated months of August 2018, October 2018, January 2019, and April 2019. In the following, we provide quantitative assessments of each criteria pollutant across different temporal periods to provide context for model performance on both fine (hourly, daily, and daily maximum) and coarse scales (monthly and annual), with diurnal profiles available in the supplement (Figure S3 in Supporting Information S1). In general, the model and observations have better agreement with longer time-averaging slices, for example, lower biases and errors. To provide greater context for our model performance, we follow EPA recommendations (Dennis et al., 2010) and compare the performance of WRF-CMAQ over our 1.3 km domain to previously published CTM studies (Table S5 in Supporting Information S1). Our comparisons use fine-scale, domain-agnostic studies (<4 km horizontal resolution), or coarser-scale (>4 km horizontal resolution) studies focused on Chicago, the Midwest, or the Great Lakes region, that is, studies with similar model domains. We select studies that use the same statistical metrics as in Table S1 in Supporting Information S1, simulate time periods after the year 2000, and integrate a similar CTM (WRF-CMAQ or WRF-Chem). We do not focus on other benchmark studies that use coarser and/or older versions of CTMs or emissions models (Emery et al., 2017; Simon et al., 2012).

error in April 2019 ($MB = 5.1\%$, $ME = 11.3$). Simulated wind speeds are biased low in each season but meet MB benchmark criteria in January 2019 and April 2019. The lowest WRF performance is shown by WD, which only meets suggested MB criteria for April 2019. Model simulated WD and station measurements are highly correlated ($r > 0.5$), except for August 2018 ($r = 0.3$). The simulation is wetter ($MB < 6\%$) and warmer ($MB < 0.8^\circ C$) than observations for all months, except for August 2018, where RH is biased low ($MB = -5.7\%$).

Within Chicago city limits, there is one NCDC meteorological station, located ~16 km inland from Lake Michigan at O'Hare International Airport on the northwestern edge of the city (denoted by a triangle in Figure 1b). Model performance in comparison to the O'Hare meteorological station is shown in Table S4 and Figure S2 in Supporting Information S1. Similar to the full 1.3 km domain comparison, meteorology in the model grid cell that contains O'Hare shows high correlations with NCDC observations for T2, WS, and RH. Also, like the full domain comparison, WRF-simulated T2 has the highest correlation with observations, while WD correlations are lowest. The ME and $RMSE$ are higher for the O'Hare grid cell for WS and RH than for the full 1.3 km domain comparison, but lower for T2 and WD. Unlike the full 1.3 km domain, simulated T2 is cooler than observations at O'Hare ($-0.2^\circ C$), though the RH biases are similar to the domain average (Table S4 in Supporting Information S1).

3.2. WRF-CMAQ Pollutant Simulation Performance

To assess WRF-CMAQ pollutant simulation performance, we compare model simulated criteria pollutant concentrations to measurements of NO_2 , O_3 , $PM_{2.5}$, SO_2 and CO from EPA Air Quality System (AQS) monitoring stations, which report hourly observations of each pollutant. Model-observation comparisons occur where WRF-CMAQ grid cells contain EPA AQS stations (Figure 1c). The number of EPA monitoring stations changes within the 1.3 km domain depending on the season with 115 total stations in August 2018, 115 in October 2018, 73 in January 2019, and 119 in April 2019. Over

Table 2
WRF-CMAQ Performance Metrics for Hourly Simulated 1.3 km (d03)
Pollutants as Compared to Environmental Protection Agency Air Quality
System Station Observations

Var	Month	μ_d	1.3 km domain performance			
			μ_p	NMB %	NME %	r
NO ₂	08/18	10.38	10.69	2.98	55.76	0.59
	10/18	10.76	11.05	2.64	66.08	0.47
	01/19	13.13	9.59	−26.95	45.45	0.62
	04/19	11.19	10.57	−5.56	51.21	0.63
	Average	11.37	10.48	−6.72	54.62	0.57
O ₃	08/18	30.28	40.25	32.92	40.04	0.69
	10/18	20.38	32.12	57.66	62.55	0.58
	01/19	24.61	31.47	27.88	34.10	0.65
	04/19	36.33	47.35	30.35	34.46	0.61
	Average	27.90	37.80	37.20	42.79	0.63
PM _{2.5}	08/18	12.12	7.49	−38.21	54.61	0.25
	10/18	6.78	7.89	16.43	67.18	0.35
	01/19	9.42	9.83	4.39	50.87	0.52
	04/19	7.60	6.26	−17.62	53.94	0.51
	Average	8.98	7.87	−8.76	56.65	0.41
SO ₂	08/18	0.76	1.41	87.23	169.66	0.21
	10/18	0.83	1.13	37.14	139.52	0.11
	01/19	0.99	1.18	19.68	110.15	0.21
	04/19	0.79	1.25	57.57	152.94	0.12
	Average	0.76	0.96	25.33	116.39	0.18
CO	08/18	250.72	204.53	−18.42	43.25	0.24
	10/18	229.61	188.81	−17.77	46.99	0.31
	01/19	284.08	186.90	−34.21	40.55	0.46
	04/19	281.43	183.51	−34.79	44.70	0.40
	Average	261.46	190.94	−26.30	43.87	0.35

Note. The average observed value is noted as μ_d , while the predicted value is noted as μ_p .

Of all pollutants, we find that WRF-CMAQ-simulated NO₂ is closest to the observations with low NMB and high correlations across months (Figure 2). The annualized average hourly correlation of NO₂ is high ($r = 0.6$; Figure 2, Table 2), while its bias is low ($NMB < -7\%$; Figure 2, Table 2). NO₂ model-observation correlations are generally greater than 0.6 regardless of temporal assessment scale, except for October 2018 (Figure 2). We find slight high biases in model simulated hourly NO₂ in August ($NMB = 3\%$) and October 2018 ($NMB = 3\%$) and low biases in January ($NMB = -27\%$) and April 2019 ($NMB = -6\%$) (Table 2). When compared to previously published WRF-CMAQ studies with different domains/resolutions, our NO₂ simulation performance exceeds NMBs and correlations reported by Bickford et al. (2014), Harkey et al. (2015), and Lawal et al., 2022.

Model-simulated O₃ is high relative to observations, with limited variation across seasons (Figure 2 and Table 2). We find that the annualized average correlation of simulated hourly O₃ is high ($r = 0.6$), but that the annualized NMB (38%) and NME (42%) are high. The highest NME for O₃ occurs in our October 2018 simulation (58%), which corresponds with the highest NME for NO₂ (64%). The lowest NMB and NME are found in January 2019 (27%, 34%), which has the lowest concentrations of O₃. Compared to other studies in the Great Lakes region, our biases and errors are higher than those of Bickford et al. (2014), who ran WRF-CMAQ without two-way coupling, and Abdi-Ouskouei et al. (2020), who used WRF-Chem. Other similar CTMs studies report O₃ biases similar to those reported here (Odman et al., 2019; Pan et al., 2017; Qin et al., 2019; Travis et al., 2016; Zhang et al., 2014). Our high O₃ bias is mainly driven by an over prediction of simulated O₃ concentrations during periods of low observed O₃, particularly at night (Figure S3 in Supporting Information S1). During warm “ozone season” months when observed O₃ is high ($O_3 > 60$ ppb), our NMB is negative (−5.4% and −7.2% for August and April) and NME are less than 17% (Table S6 in Supporting Information S1). When our model performance evaluation is limited to hours when observed O₃ concentrations are greater than the 50%ile value, average annualized NMB is reduced to ~25% (Table S6 in Supporting Information S1). Lastly, and further confirming WRF-CMAQ's challenges with capturing low O₃ concentrations, the NMB in our model-simulated daily maximum 8-hr running average O₃ (MDAO₃) is ~27% when annualized, ~25% in O₃ season months, and only ±2% when MDAO₃ is greater than 60 ppb (Table S6 in Supporting Information S1).

Unlike model simulated O₃, our simulated hourly PM_{2.5} concentrations have low biases and low correlations (Figure 2 and Table 2). The annualized average correlation of hourly PM_{2.5} is 0.4, with NMB of −10% and NME of 56%. August 2018 hourly PM_{2.5} has the largest bias (−38%) and lowest correlation ($r = 0.25$), while the highest NME (67%) and highest positive NMB (16%) are found in October 2018. Within the Great Lakes region, we find that our model-observation agreement for PM_{2.5} has higher correlations and similar NMEs to Bickford et al. (2014). Compared to other WRF-CMAQ studies within the continental U.S., our PM_{2.5} NME is lower than Hogrefe et al., 2015 but higher than Liu et al., 2010 and Wang et al., 2021. Our PM_{2.5} NMB and MB are similar to Hogrefe et al. (2015) and Wang et al. (2021), but lower than Liu et al., 2010 and Torres-Vazquez et al., 2022.

The agreement of our model simulated SO₂ and CO compared to the AQS observations were the lowest of the 5 criteria pollutants (Figure 2 and Table 2). Annualized average correlation of SO₂ is 0.18, with NMB = 25% and NME = 116%. Annual average correlation of CO is 0.35, with NMB = −26% and NME = 44%. Few previous WRF-CMAQ studies report their performance of SO₂ and CO. Compared to those that do, our simulation of SO₂ had lower NMBs, higher NMEs, and lower correlations (Bickford et al., 2014; Campbell et al., 2019).

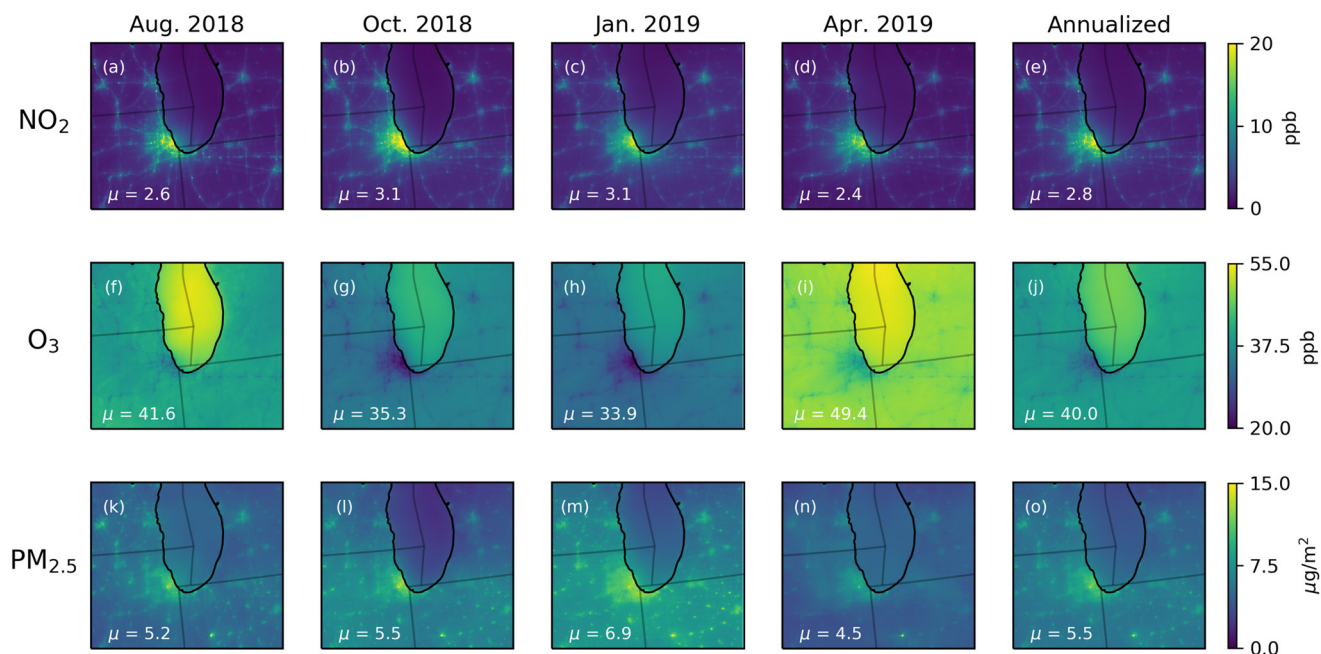


Figure 3. Monthly and annualized average WRF-CMAQ simulated NO₂ (a–e), O₃ (f–j), and PM_{2.5} (k–o) for the 1.3 km simulation domain (d03). From left-to-right each column presents August 2018, October 2018, January 2019, and April 2019, with the domain-average (μ) concentrations annotated in the lower left of each panel. The right-most column provides the annualized average. Note: the colorbar for O₃ concentrations begins at 20 ppb.

3.3. Domain-Wide Characterization of WRF-CMAQ Simulated Pollutants

In Figure 3, we show monthly-average simulated NO₂, O₃, and PM_{2.5} concentrations over the 1.3 km domain (d03) for each season (Figure S4 in Supporting Information S1 shows model results overlaid with station observations). Simulating pollutants at a 1.3 km spatial resolution facilitates the characterization of distinct urban-rural patterns, the influence of Lake Michigan on regional O₃ distributions, pollutant hotspots over highway corridors, stationary emitting sources, and urban centers. We distinguish urban areas from rural by classifying the most populated census tracts (>95%ile) from the American Community Survey 2018 (Manson, Steven et al., 2022) as urban, and all other areas as rural (Figure S5 in Supporting Information S1). In the following, we individually discuss domain-wide analyses of each pollutant and then highlight the model's characterization of pollutants within the city of Chicago.

The simulated NO₂ concentrations largely track high-population areas and highway corridors (Figures 3a–3e). In all seasons, the interstate highway system that connects population centers is highlighted by the interconnected system of roadways with elevated NO₂ concentrations. The lowest NO₂ concentrations in our domain are simulated over northernmost and easternmost portions of Lake Michigan, in areas distant from emissions sources. Likewise, rural areas distant from roadways have low NO₂ concentrations. We find that the average annual urban concentration of NO₂ in our domain is simulated to be 3.5 ppb (59.8%) higher than average concentrations in rural portions of our domain (Figure 3 and Table S7 in Supporting Information S1). Across seasons, domain-wide NO₂ concentrations correspond with the magnitude of simulated NO_x emissions (Figure S6 in Supporting Information S1). In January 2019, domain average NO₂ concentrations are highest ($\mu = 3.1$ ppb; Figure 3c), which corresponds to our highest simulated NO_x emissions ($\mu_{\text{NOx,January}} = 2.6 \times 10^{-3}$ g/s). The lowest domain average NO₂ concentrations occur in April 2019 ($\mu = 2.4$ ppb; Figure 3d), which co-occurs with low NO_x emissions ($\mu_{\text{NOx,april}} = 2.5 \times 10^{-3}$ g/s).

In contrast to NO₂, O₃ concentrations are simulated to be relatively low over urban areas and roadways, with low concentrations over individual highway corridors apparent (Figures 3f–3j). Across seasons, the spatial distribution of O₃ concentrations is relatively consistent, however the magnitude of O₃ concentrations varies by season. Of the 4 months that we simulate, we find that the highest O₃ concentrations occur in April 2019 ($\mu = 49.4$ ppb; Figure 3i), while the lowest concentrations are simulated in January 2019 ($\mu = 33.9$ ppb; Figure 3h). Over simulated warm season months (i.e., April 2019 and August 2018), we find that domain-wide O₃ concentrations

are ~ 1.5 times higher than cool-season concentrations. Comparing concentrations across the urban-rural divide (Figure S5 in Supporting Information S1), we find that O_3 over urban areas is simulated to be ~ 3.3 ppb (9.4%) lower than over rural areas, with the greatest urban-rural difference in cool season months (Table S7 in Supporting Information S1).

Across all seasons, the highest simulated concentration of O_3 in the 1.3 km domain occurs over Lake Michigan (Figures 3f–3j). The simulation of elevated over-lake O_3 concentrations is consistent with previous Lake Michigan observation and modeling campaigns (Doak et al., 2021; Dye et al., 1995; Foley et al., 2011), and similar to other studies focused on inland bodies of water (e.g., Chesapeake Bay, Goldberg et al., 2014). Elevated O_3 over Lake Michigan is thought to be dependent on the circulation of primary pollutants from land to lake via the lake-breeze. Elevated O_3 over the lake occurs through the following idealized sequence of events: (a) In the morning land-based emissions (O_3 precursors) are transported over the lake by a land-breeze, which combine with shipping emissions, and are trapped within a shallow boundary layer. (b) As the day warms, the land-lake temperature gradient weakens, and the land breeze dwindles. Fewer NO_x emissions are transported to the lake. (c) As sunlight increases, photochemical production of O_3 over the lake is enhanced. Due to the low number of depositional pathways over the lake, O_3 accumulates. (d) On days where a lake breeze forms, O_3 is advected inland, often to areas where the original precursor emissions did not originate. Lake breeze effects are primarily a warm season phenomenon, however, the low concentration of over-lake depositional pathways also contributes to elevated cool season O_3 concentrations (Figures 3f–3j) (Doak et al., 2021; Dye et al., 1995). In our simulations, land-lake O_3 concentration differences are greatest in August 2018, as the average concentration of O_3 over land (39.8 ppb) is 11 ppb lower than the average O_3 concentration over the lake (50.4 ppb).

Domain-wide simulated $PM_{2.5}$ concentrations show greater spatial smoothness, such that elevated $PM_{2.5}$ hot spots have a more diffusive footprint compared to NO_2 hot spots (Figures 3k–3o). Across months, the spatial pattern of simulated $PM_{2.5}$ concentrations is relatively consistent and largely tied to the location of emission sources. Despite consistent spatial patterns across months, the relative magnitude of $PM_{2.5}$ concentrations is influenced by meteorological conditions (e.g., boundary layer height and wind speeds), the magnitude of seasonal primary PM emissions, and secondary PM pollutant formation reactions. The domain-wide average concentration of $PM_{2.5}$ peaks in January 2019 ($\mu = 6.9 \mu/m^3$) and is lowest in April 2019 ($\mu = 4.5 \mu/m^3$), which mirrors the pattern of emissions of PM and its precursors (Figure S6 in Supporting Information S1). Both stationary and mobile sources of $PM_{2.5}$ typically co-emit NO_x emissions, as such simulated $PM_{2.5}$ hotspots tend to co-occur with NO_2 hotspots over urban areas, highways, and stationary sources (Figures 3a–3e and 3k–3o). However, compared to NO_2 , $PM_{2.5}$ concentrations are more spatially diffuse due to the longer atmospheric lifetime of PM species (Laughner & Cohen, 2019; Pinto et al., 2004). Further, the urban-rural concentration disparity is lower, that is, $PM_{2.5}$ concentrations are 22% higher in urban v. rural areas, compared to 60% for NO_2 (Table S7 in Supporting Information S1). Simulated grid cells with the highest concentration of $PM_{2.5}$ occur outside of urban areas and are primarily associated with emissions from industrial and manufacturing point sources.

3.4. Neighborhood-Scale Characterization of WRF-CMAQ Simulated Pollutants

Our domain-wide analysis demonstrates the ability of the 1.3 km WRF-CMAQ simulations to characterize differences in urban-rural regimes and identify pollutant hotspots, however it does not highlight the ability of the model to resolve and characterize neighborhood-scale air quality. To demonstrate this ability, we provide an in-depth analysis of a sub-region of the 1.3 km modeling domain, that is, the city of Chicago (Figure 4a), a city with ~ 2.7 million people (Manson, Steven et al., 2022). At the 1.3 km model resolution, there are on average ~ 5 grid cells in each of the 77 neighborhoods that comprise the city (Figure 4). Chicago sits close to the center of our 1.3 km domain, and in Figure 3 is identifiable as both an NO_2 and $PM_{2.5}$ hotspot at the southwest corner of Lake Michigan. Major sources of emissions within Chicago include transportation, industry, and buildings. The city has six major interstate highways (I-290, I-294, I-90, I-94, I-55, I-57) that loosely outline the City's lakeside central business district or "Loop." There are two airports within City limits, O'Hare in the northwest and Midway in the south central. Most industrial activities occur on the west and southwest sides of the city.

In Figures 4b–4d, we show the city's average annualized concentrations of NO_2 , O_3 , and $PM_{2.5}$. Simulated concentrations of criteria pollutants are higher within Chicago than the domain average, so Figure 4 has a different color bar than that used in Figure 3. For all pollutants, the 1.3 km WRF-CMAQ simulations reveal substantial spatial heterogeneity amongst neighborhoods. Spatial gradients are particularly substantial for simulated NO_2 ,

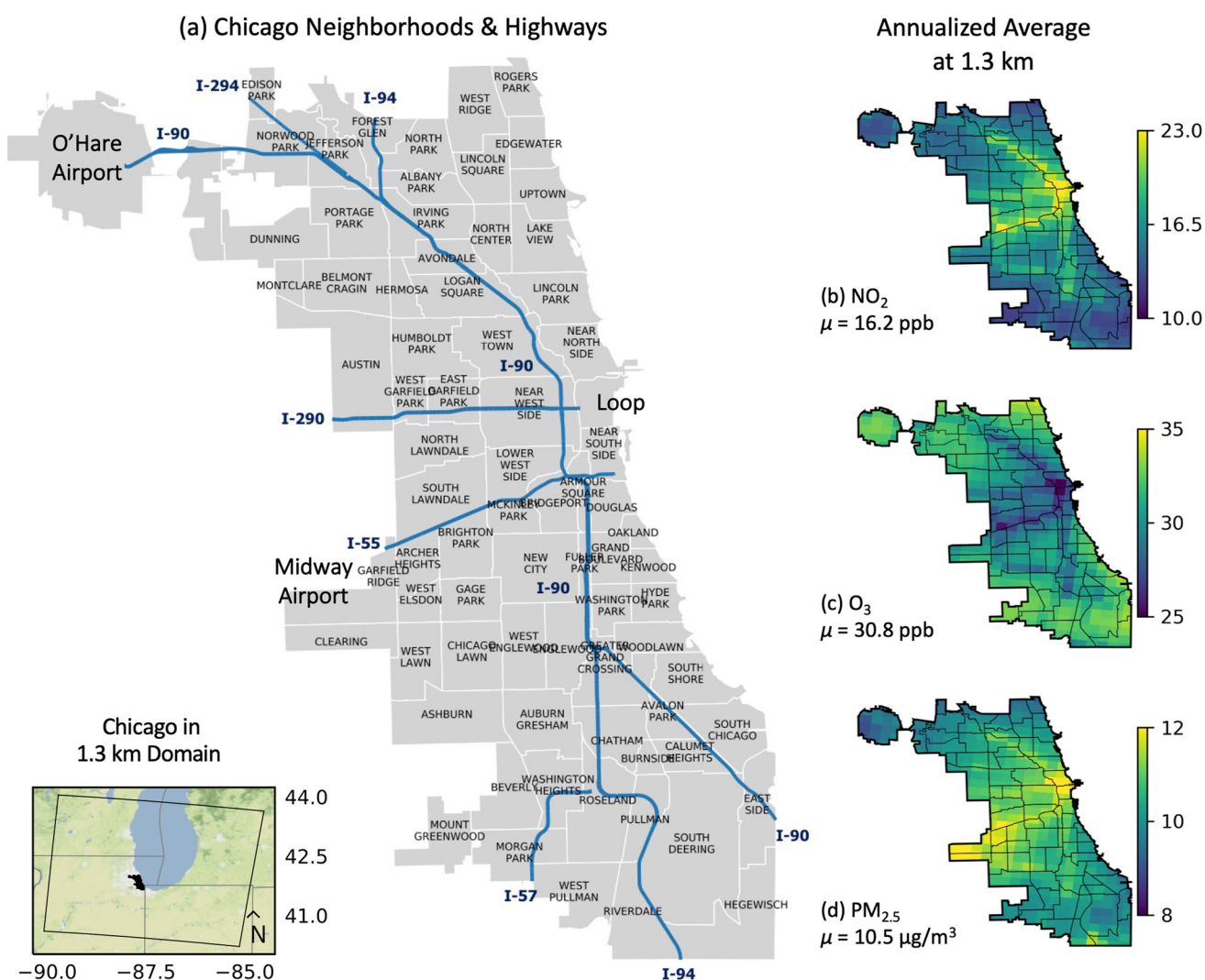


Figure 4. Chicago geography and simulated pollutants. (a) Neighborhoods and highways within the city of Chicago. Inset at lower left depicts the location of Chicago (black) within the 1.3 km domain. In the right column, we provide annualized WRF-CMAQ simulated (b) NO_2 , (c) O_3 , and (d) $\text{PM}_{2.5}$ concentrations over Chicago and average concentrations within city limits (μ).

with concentrations in some neighborhoods double those in others. The predominant spatial pattern of simulated pollutants strongly corresponds to the interstate highway system (Figure 4a), although the highest concentrations of NO_2 and $\text{PM}_{2.5}$ are simulated where the lowest concentrations of O_3 are simulated. O_3 concentrations are elevated in neighborhoods that abut Lake Michigan, consistent with the influence of the lake breeze, and in neighborhoods without interstate highways. In the following paragraphs we discuss annualized pollutant pattern details across Chicago, as well as patterns of individual months. We determine “highest” or “lowest” values of pollutant concentrations by computing the 95%ile or 5%ile values, respectively.

The highest annualized concentrations of NO_2 (where $\mu_{\text{annual}} > 19.5 \text{ ppb}$) are simulated on the West side of Chicago and in the Loop, where highways are prevalent (e.g., I-90, I-290, and I-55) and simulated NO_x emissions are high (Figure S6 in Supporting Information S1). The lowest NO_2 concentrations (where $\mu_{\text{annual}} < 11.3 \text{ ppb}$) are simulated in the lake-front neighborhoods, with the exception of those in the Loop. Lakefront neighborhoods are east of the main interstate highways, where lower NO_x emissions and ventilation contribute to the relatively low simulated NO_2 (Figure S6 in Supporting Information S1). Across seasons, NO_2 concentrations within Chicago remain highest over the 3 most-trafficked inter-state highways: I-290, I-90, and I-94 (Figure 4b). Simulated NO_2 concentrations are lowest in April 2019 ($\mu = 14.2 \text{ ppb}$) and highest in October 2018 ($\mu = 18.7 \text{ ppb}$), although the greatest NO_2 bias was also found in October 2018. Compared to the full model domain ($\mu_{\text{domain}} = 2.4\text{--}3.2 \text{ ppb}$;

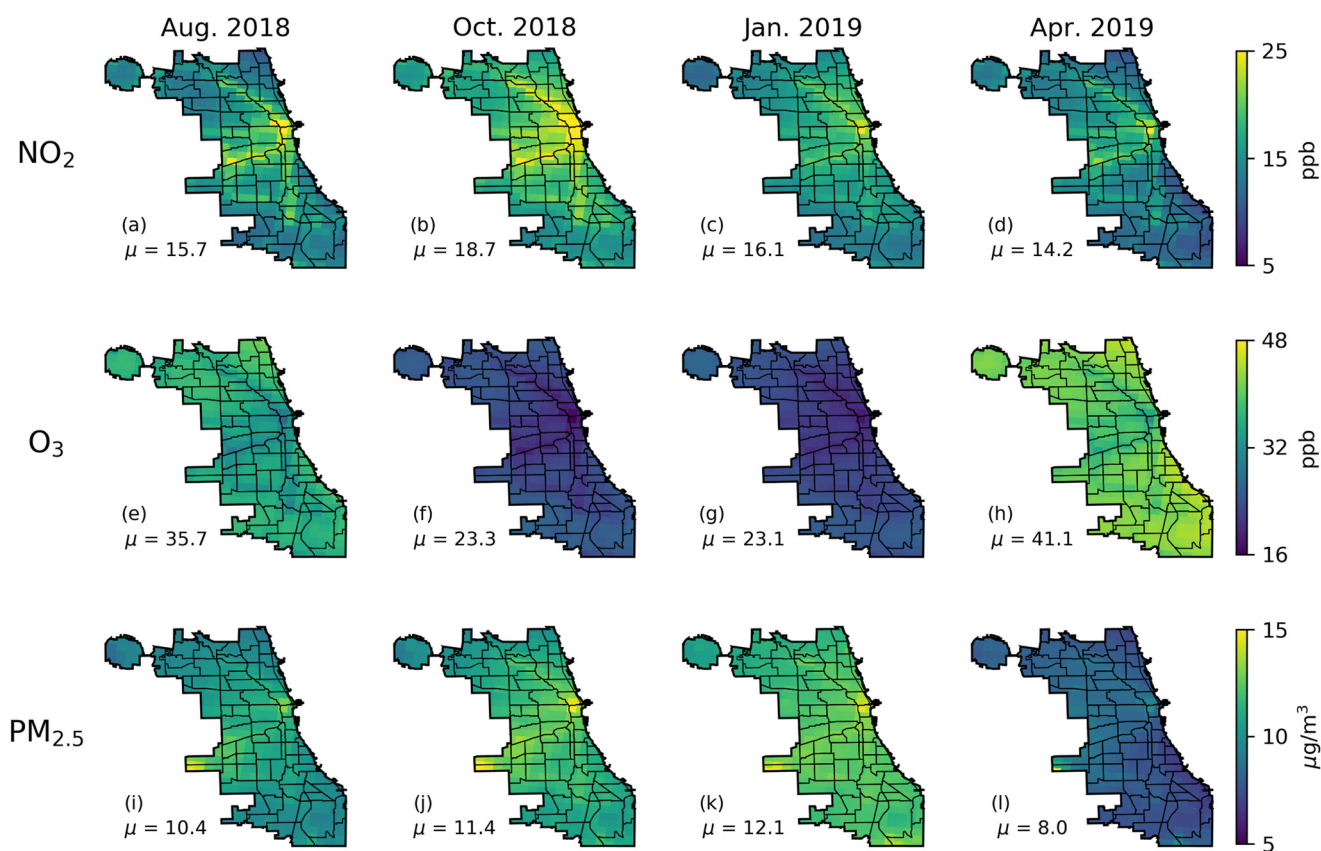


Figure 5. Monthly average NO₂ (a–d), O₃ (e–h), and PM_{2.5} (i–l) concentrations over Chicago, as simulated in the 1.3 km domain. Columns depict August 2018, October 2018, January 2019, and April 2019 simulations. Chicago-average concentrations are annotated (μ).

Figures 3a–3d, average NO₂ over Chicago is nearly five times higher ($\mu_{\text{Chicago}} = 14.2\text{--}18.7$ ppb) across seasons (Figures 5a–5d). Unlike the NO_x–NO₂ emission–concentration relationship found over the full domain, we find that average NO₂ concentrations over Chicago do not correspond with emission magnitude differences, as Chicago NO_x emissions are lowest in August 2018 and highest in January 2019 (Figure S6 in Supporting Information S1), while NO₂ concentrations are highest in October 2018 and lowest in April 2019. We discuss this disconnect further in our discussion of model performance in Section 4.1.

Simulated annualized and individual month O₃ concentrations within Chicago tend to be the spatial inverse of simulated NO₂ concentrations (Figures 4 and 5). The lowest concentrations ($\mu_{\text{annual}} < 28.5$ ppb) of O₃ are simulated on the West side of the city, near the interstates. These locations are also simulated to have the highest NO₂ concentrations, that is, O₃ is suppressed via titration by NO. O₃ concentrations are highest in the warm months, with August 2018 ($\mu = 35.7$ ppb) and April 2019 concentrations ($\mu = 41.1$ ppb) nearly double October 2018 ($\mu = 23.3$ ppb) and January 2019 concentrations ($\mu = 22.7$ ppb). Average annualized O₃ concentrations in Chicago ($\mu_{\text{annual}} = 30.7$ ppb) are simulated to be significantly lower than the domain average because of the lake reservoir of O₃ ($\mu = 40.0$ ppb). Even when land-only O₃ concentrations are isolated, Chicago has concentrations that are slightly lower than the rest of the full model domain ($\mu_{\text{land, domain, annual}} = 38.8$ ppb). Warm-season O₃ is highest near Northern lake-front neighborhoods, which are distant from the major interstates, have low NO_x emissions (Figure S6 in Supporting Information S1), and subject to lake breeze advection of the reservoir of O₃ over Lake Michigan. In the cool months, O₃ concentrations are simulated to be highest on the western edges of the city. However, the cooler months have a lower range of O₃ concentrations (± 8.9 ppb) than warmer months (± 15.5 ppb).

Annualized PM_{2.5} concentrations in Chicago correspond well with the spatial patterns of the interstate system, though the PM_{2.5} footprint is spatially more extensive than that of NO₂ (Figure 4). PM_{2.5} concentrations in Chicago are simulated to be two times higher than the average concentration of the full model domain

($\mu_{\text{domain,annual}} = 5.5 \mu\text{g}/\text{m}^3$, $\mu_{\text{Chicago,annual}} = 10.2 \mu\text{g}/\text{m}^3$). $\text{PM}_{2.5}$ concentrations peak on the west side of Chicago near Midway airport and the intersection of I-290 and I-55 with I-90 ($\mu = 12\text{--}13 \mu\text{g}/\text{m}^3$). The lowest concentrations of $\text{PM}_{2.5}$ occur on the lakefront ($\mu = 8\text{--}10 \mu\text{g}/\text{m}^3$). Similar to O_3 , Chicago $\text{PM}_{2.5}$ levels show strong seasonal variations, though the simulated concentrations of $\text{PM}_{2.5}$ are highest in the seasons when O_3 is lowest. As such, simulated $\text{PM}_{2.5}$ peaks in the cooler months (Figures 5j and 5k) and is lowest in April 2019 ($\mu = 8 \mu\text{g}/\text{m}^3$). Areas of high $\text{PM}_{2.5}$ in Chicago are consistent across seasons, in particular on the west side of the city and within the Loop.

3.5. Benefits and Disbenefits of Increased Model Resolution

Our nested modeling framework facilitates assessment of the potential benefits and/or disbenefits of attempting to resolve neighborhood scale meteorology and air pollutants with a CTM. That is, given that our methodology simulates atmospheric chemistry and meteorology at both 4 and 1.3 km resolutions, an assessment of increased spatial resolution on model performance is possible. However, our chosen methodology does not provide a pure spatial resolution sensitivity analysis, that is, while the underlying emissions data of each simulation is the same (NEI 2016v1), the meteorologically informed emissions are slightly different due to differences in the 4 and 1.3 km WRF simulations. Further, we compare stations to grid cells in each domain, and the 1.3 km grid cells cover a smaller area than the 4 km grid cell. Despite this imperfect sensitivity analysis, we compare model performance at both resolutions. We restrict our comparison to model performance over the 1.3 km domain. As such, we use the same 10 NCDC meteorological observing stations and the ~ 125 EPA AQS stations shown in Figure 1 and discussed in the WRF-CMAQ simulation comparison. After this performance comparison, we investigate spatial changes in simulated pollutants over Chicago at the different resolutions.

For the simulated meteorology, we find that the increase in resolution benefits the performance of WS and WD, has no influence on RH, and has disbenefits for T2 (Table 1 and Table S8 in Supporting Information S1). Higher resolution provides the greatest benefit to simulated WD as MB and ME are lower at 1.3 km and correlations are higher. In contrast, we find that observed T2 is better captured in the 4 km simulation, as lower bias and error and higher correlations are found compared to the 1.3 km simulation. Within Chicago (with just one NCDC station) the 1.3 and 4 km simulations perform similarly to their domain-wide performance, with WD showing slightly lower biases in the 4 km domain (Table S9 in Supporting Information S1).

For simulated pollutant concentrations we find higher model-observation correlations in the higher resolution (1.3 km) simulation, though this improvement is coupled with increased ME (Table S10 in Supporting Information S1). The 1.3 km simulation showed higher correlations than the 4 km simulation for all criteria pollutants, though this increase was marginal ($\Delta r < 0.1$, Table S10 in Supporting Information S1). The 1.3 km simulation of NO_2 has a closer agreement to the EPA stations, but this comes with slightly higher normalized errors (+0.25%; Table S10 in Supporting Information S1). On average, the 1.3 km simulation NMB was lower than that of the 4 km model simulation for each season, which came at a trade-off, as NME was only lower in the 1.3 km simulation in April 2019. The correlation between AQS observation and model outputs for NO_2 were similar for the 1.3 and 4 km simulations. The 1.3 km simulation lowered the NMB by 8% in August 2018 and January 2019, with marginal bias improvement in April 2019 and January 2019. In contrast, the 1.3 km simulation of O_3 showed higher NMB and NME than the 4 km simulation. For $\text{PM}_{2.5}$, we find that the 1.3 km resolution simulation has a lower NMB than the 4 km simulation for three out of four seasons, but the NME is marginally higher (0.9%) in the higher resolution simulation. Simulated SO_2 showed the largest improvement with finer model resolution ($\Delta\text{NMB} = 10\%$, $\Delta r = 0.03$), however this was also the pollutant with the lowest performance in both the 1.3 and 4 km domains. CO had slightly better performance in the 4 km domain, as the NME and NMB were 0.5%–1% higher, respectively, in 1.3 km simulation.

These meteorological and pollutant performance analyses are limited due to the low number of sensors relative to the number of grid cells simulated in our modeling domain (125 EPA stations and 10 NCDC stations vs. 90,720 grid cells). In addition, the finer resolution creates opportunities for local-scale meteorological processes to influence agreement, particularly for pollutants which are not well mixed in the atmosphere (Zhang et al., 2014). The measurement-prediction relationship can be greatly influenced by model grid cell size, plumes, and wind speeds and directions. For example, while the relative amount of SO_2 simulated in a plume may be correct, due to the increase in the number of grid cells in a higher resolution simulation, the potential for an erroneously simulated WD to adversely influence model grid cell-observation fidelity increases.

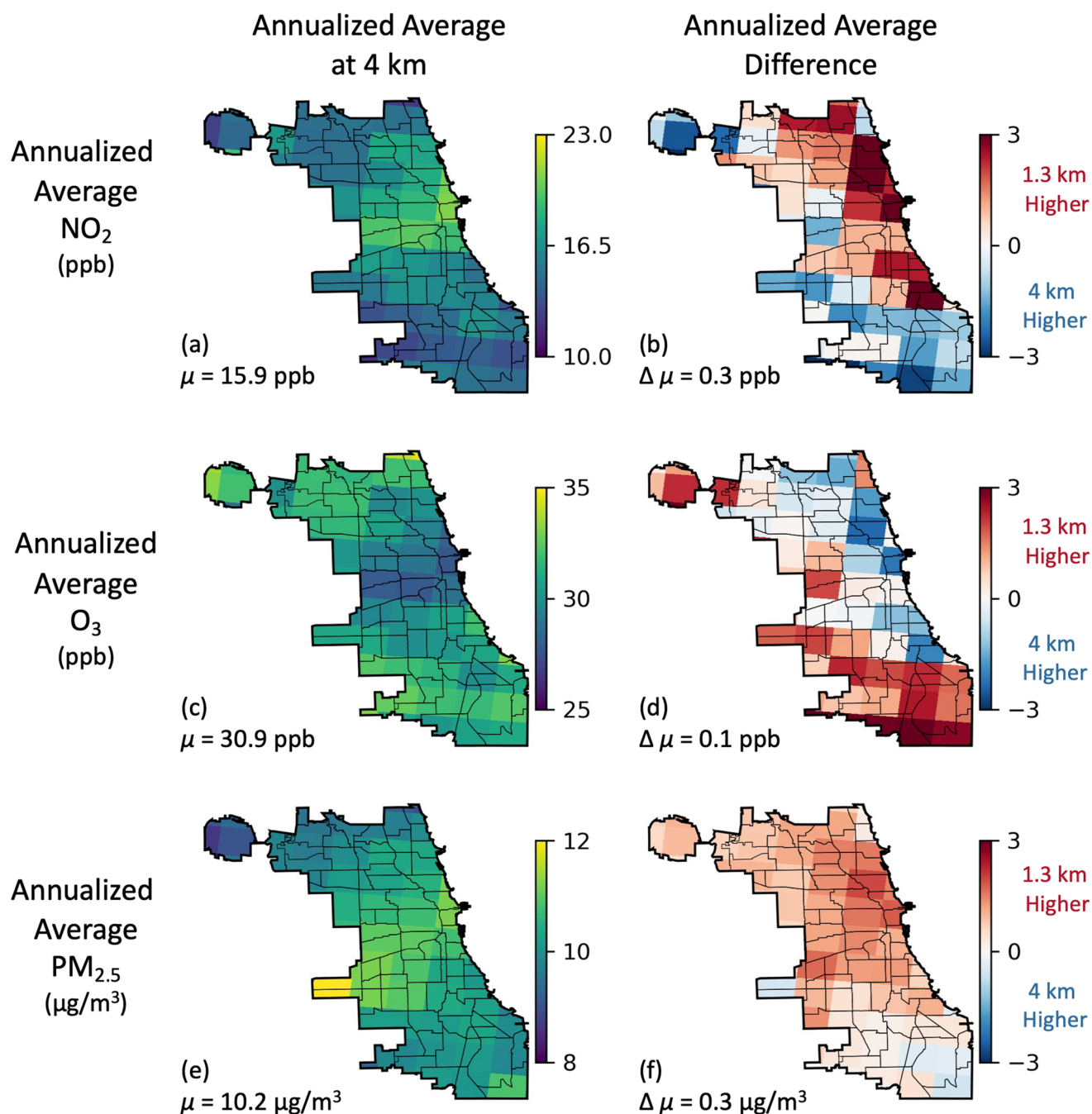


Figure 6. Average annualized NO₂ (a), O₃ (c), and PM_{2.5} (e) within Chicago city limits as simulated in the 4 km simulation. (b, d, f). Relative pollutant differences between 1.3 and 4 km resolution simulations. Average Chicago concentrations (μ) and average differences between model resolutions ($\Delta \mu$) are annotated.

While model performance when assessed against very limited station observations demonstrates improvement (albeit marginal) when the model resolution increases from 4 to 1.3 km, we note that a key advantage of our higher resolution simulation is the ability to characterize neighborhood-scale air quality, particularly within intra-urban environments. As Chicago is the densest metropolitan area in our modeling domain, we focus our analysis on air quality differences between the 1.3 and 4 km simulations within city limits. We find that over Chicago the 1.3 km simulation has higher average NO₂, PM_{2.5}, and O₃ concentrations than the 4 km simulation (Figure 6). Differences in pollutant concentrations at different model resolutions can be caused by a number of factors, including

differences in the underlying emissions data, differences in simulated micro-scale meteorology, and/or the nuances of emission-chemistry interactions at the grid cell level. In the following, we provide examples of each.

The overall higher concentrations of NO_2 and $\text{PM}_{2.5}$ simulated over Chicago at 1.3 km are in part due to differences in the underlying meteorologically-informed emissions. In the case of NO_2 , the difference in domain average emissions over the 1.3 km domain and the corresponding subset of the 4 km domain is 0, as the net flux of emissions is the same between the two. However, isolating subsets of the domains does not result in the same balance, as shown in the Chicago subset of emissions (Figure S6 in Supporting Information S1) and resulting pollutant concentration differences (Figure 6). Emissions are different between the 1.3 and 4 km domains because the WRF-simulated temperatures and relative humidities are different at the grid cell level which affects the emissions processing (Figure S7 in Supporting Information S1). These differences are particularly apparent near the lake shore, where the level of detail afforded by the 1.3 km grid (Figure S8 in Supporting Information S1) results in notable emission differences (Figure S7 in Supporting Information S1). Specifically, we find that over Chicago, emission rates of NO_x , organic and elemental carbon, and VOCs are 7.5%, 6.2%, and 1.5% higher in the 1.3 km emissions relative to the 4 km emissions. These higher emission rates, in part, explain the higher average concentration of pollutants over Chicago. For example, elevated NO_x and PM species emissions over the city center and highways (Figure S7 in Supporting Information S1), contribute to higher NO_2 and $\text{PM}_{2.5}$ concentrations in the 1.3 km simulation (Figure 6). For O_3 , it is likely that higher relative NO_x emissions at 1.3 km suppress O_3 concentrations via enhanced NO titration compared to the 4 km simulation.

Despite the above, we find that differences in emissions do not always result in corresponding and co-located changes in pollutant concentrations. As an example, we highlight near-lake grid cells on the north side of Chicago where 1.3 km NO_x emissions are lower than at 4 km, but the resulting NO_2 pollutant concentrations are higher (Figure S7g–S7j in Supporting Information S1). Similarly, on the south side of Chicago we note grid cells with higher NO_x emissions at 1.3 km, but lower NO_2 concentrations than simulated at 4 km. This finding is notable because it suggests that fine-scale differences in simulated meteorology drive nonlinear outcomes that affect the production and destruction of pollutants, and is indicative of the value added by fine-scale, fully-coupled CTMs. This finding also suggests caution should be taken when assessing health and justice outcomes at neighborhood scales, particularly if the methods employed do not include dynamic meteorological processes.

3.6. O_3 Regimes Over the Domain

One notable feature of our 1.3 km simulation is the ability to characterize the O_3 regime at fine spatial resolutions. Localized formation of tropospheric O_3 is a nonlinear process that depends on the relative abundances of precursor emissions, the transport of O_3 and other precursor emissions from upwind areas, and the scale and magnitude of local sinks. Despite this complexity, O_3 production environments are often simplified as either NO_x - or VOC-limited regimes (Kleinman, 1994; Sillman et al., 1990). An area is considered “ NO_x -limited” when VOCs are more available than NO_2 , and as such, O_3 production is limited by the radical termination of NO_2 by OH. O_3 production is “VOC-limited” when NO_x is abundant, and O_3 production is limited by the availability of peroxy radicals from VOC oxidation (Schroeder et al., 2017). To determine if areas are NO_x - or VOC-limited, VOC concentrations can be compared to NO_x concentrations (Ashok & Barrett, 2016). The resultant ratio serves as a proxy to describe the chemical loss of $\text{HO}_2 + \text{RO}_2$ (LRO_x) over the chemical loss of NO_x (LNO_x) (Schroeder et al., 2017). Given limited surface observations, researchers often turn to columnar ratios of HCHO to NO_2 from remotely sensed instruments like TropOMI to provide spatially continuous estimates of O_3 regimes (Ashok & Barrett, 2016). While there are not definitive VOC: NO_x or HCHO: NO_2 ratio values to delineate whether an area is NO_x - or VOC-limited, it is generally accepted that very low ratios (e.g., $< \sim 1$) indicate an area is VOC-limited, very high ratios (e.g., $> \sim 2$ for column, $> \sim 7$ for surface over Chicago) indicate an area is NO_x -limited, and values between the high and low range are considered “transitional” (Ashok & Barrett, 2016; Jin et al., 2017). Despite the above context, regime thresholds are uncertain and can be influenced by a number of factors, including local meteorology and VOC species composition (Rethinking the Ozone Problem in Urban and Regional Air Pollution, 1991; Seinfeld & Pandis, 2016).

Several previous studies using a variety of methods have attempted to characterize the Chicago region's O_3 regime. These studies have arrived at different conclusions over the years, including some that have found Chicago to be NO_x -limited (Laughner & Cohen, 2019), VOC-limited (Blanchard et al., 2008; Koplitz et al., 2022), or in a transitional state (Jin et al., 2020; Jing & Goldberg, 2022). In Figure 7 and Table S12 in Supporting Information S1, we

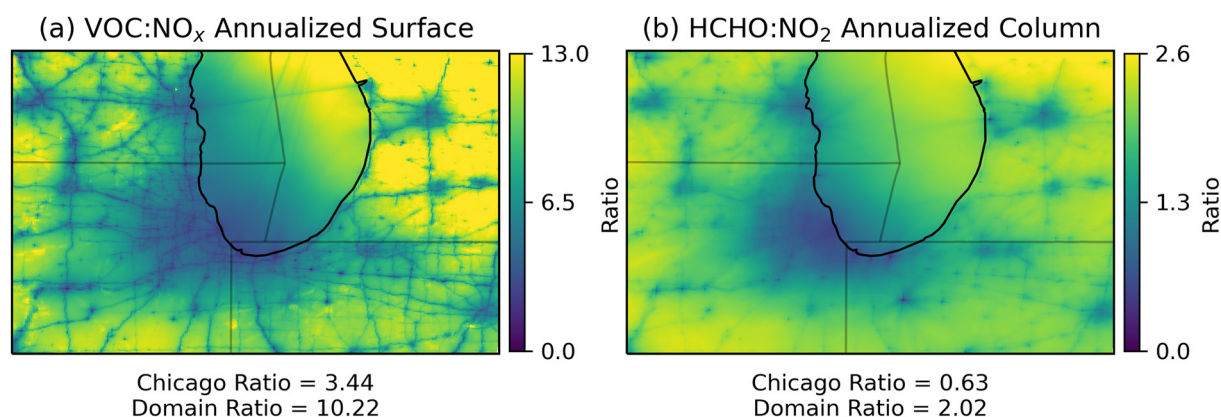


Figure 7. Daytime (7 a.m.–7 p.m.) annualized average of the (a) VOC:NO_x surface ratio and (b) HCHO:NO₂ column ratios over the 1.3 km domain.

provide WRF-CMAQ simulated annualized daytime (7 a.m.–7 p.m.) surface VOC:NO_x and column HCHO:NO₂ ratios. We find substantial detail and heterogeneity in simulated surface-level VOC:NO_x ratios (Figure 7a), although the simulated column average HCHO:NO₂ ratio shows similar spatial patterns (Figure 7b). The more diffuse spatial gradients in the column are due to the integration of the chemicals through the simulated troposphere. The greatest difference between the surface-level and column ratios are shown in the finer characterization of highways and population centers, which show high NO_x saturation at the surface (Figure 7). Both the domain average annualized VOC:NO_x and HCHO:NO₂ ratios are higher over the full 1.3 km domain than over Chicago, indicating that while the full domain is NO_x limited, the annualized city regime is VOC-limited to transitional. To provide finer temporal detail, we characterize the O₃ regime for each simulated month. Similar to Ashok and Barrett (2016), we find that the surface and column ratios change with the season (Figures S9 and S10 in Supporting Information S1). Domain-average surface ratios range from ~7.0–18.5 suggesting a NO_x-limited regime in all months (Figure S9 in Supporting Information S1), while column average ratios range from ~0.6 to 4.3, indicative of a more seasonally dynamic environment (Figure S10 in Supporting Information S1). Over Chicago, the surface ratios range from ~3.0–4.6, firmly in the transitional regime (Figure S9 in Supporting Information S1), while column ratios span ~0.2–1.3 indicative of a VOC-limited to transitional regime (Figure S10 in Supporting Information S1). Given the diversity of previous findings and fundamental uncertainties in regime thresholds, it is perhaps not unexpected that our regime determinations are somewhat sensitive to methodological choice. Despite these uncertainties, the detail afforded by the 1.3 km surface ratio plots is notable (Figure 7a and Figure S9 in Supporting Information S1), both for its contrast with column-based characterizations and its potential in O₃ abatement investigations. We find that the simulated surface O₃ ratio has a spatial gradient that changes over relatively short distances. The consequence of this finding, and its effect on policy design for O₃ precursor control alludes to the complexity of the system and the benefits of resolving atmospheric chemistry and pollutants at the neighborhood-scale.

4. Discussion

In the above we present the first neighborhood-scale (1.3 km) two-way coupled WRF-CMAQ simulations focused on the southern Lake Michigan-Chicago region. We perform hindcast simulations of individual months from each season and assess the model's performance against meteorological and pollutant station observations, as well as against coarser resolution (4 km) simulations. Below we summarize our results and discuss notable findings and experimental caveats.

4.1. Summary of Model Performance

In our WRF-CMAQ simulations, we show that the WRF-simulated meteorological variables WD, WS, and T2 meet performance criteria suggested by Emery and Tai (2001). The lowest performing simulated meteorological variable is WD, a variable that models have historically struggled to reproduce with high fidelity and which has previously been shown to be sensitive to model resolution, boundary layer parameterization, and land cover schemes (Carvalho et al., 2012). In our simulations, we find that WRF-CMAQ best-captures observed WD in

January 2019 and October 2018, but struggles in August 2018 and April 2019, likely due to more diffuse warm season winds, similar to findings presented in Zhang et al. (2014). In addition, recent WRF simulations have demonstrated the influence of different lake temperature datasets on meteorology, particularly air temperatures and convection, in domains near to Lake Michigan (Wang et al., 2022). Future work should assess the role of lake temperatures, and uncertainties therein, on the simulation of pollutants.

In the CMAQ portion of our two-way coupled WRF-CMAQ simulation, NO₂ concentrations show the best performance when compared against EPA criteria pollutant AQS station observations, including high correlations and low biases and errors. However, we note that over Chicago (Figure 6) and at EPA stations (Table 2), the highest concentration of NO₂ is simulated in October 2018, in contrast with NO_x emissions which peak in January 2019 (Figure S6 in Supporting Information S1). This mismatch is likely a consequence of model biases. In January 2019, the NO₂ bias over the domain and at the nearest Chicago AQS Station (17-031-3103) is highest and negative (*NMB* = −26%). The relatively large negative January NO₂ bias is likely driven by an anomalously large negative bias in simulated RH compared to other months (i.e., domain-average RH *MB* is −7.5% and Chicago RH *MB* is −15%). The January NO₂ negative bias is found to be largest in the early morning hours, which is coincident with the simulated RH bias maximum (Figures S1–S3 in Supporting Information S1). Previous studies have demonstrated that lower RHs are associated with lower concentrations of NO₂ (Harkey et al., 2015). It is also notable that October 2018, the month with the highest simulated concentration of NO₂ over Chicago, and lowest, but positive *NMB* (2.6% over all stations, 4.2% at station 17-031-3103), shows the largest night-time buildup of NO₂ and O₃ (Figure S3 in Supporting Information S1), which is likely caused by low night-time titration (Sharma et al., 2017). Low night-time titration has previously been demonstrated to be a consequence of weak vertical mixing in the ACM2 PBL scheme (Zhao et al., 2019).

Similar to NO₂, we find high correlations between observed and simulated O₃ concentrations, which reflects the strong anticorrelated relationship between O₃ and NO₂. However, unlike NO₂, O₃ is biased high across all seasons, with the largest biases occurring at night (except for January 2019). Previous studies have found that applying the ACM2 PBL scheme may contribute to excess nighttime vertical mixing, which can dilute NO concentrations at the surface and reduce O₃ titration as well as transport ozone from the residual layer to the surface, both of which contribute to higher nighttime O₃ concentrations (J. Hu et al., 2016; Sharma et al., 2017). Transport from boundary conditions likely contribute to the high bias as well. We find that surface-level O₃ in CAM-Chem is consistently biased high, particularly at night (Table S13 in Supporting Information S1) which would contribute excess O₃ transport into our d02 (4 km) simulation domain. Previous studies have found that an overestimation of NO_x emissions can contribute to excess O₃ (Qin et al., 2019; Travis et al., 2016), however in our simulations NO₂ is biased low or negative on average (Table 2). Future studies could address the simulated O₃ biases by running sensitivities which target boundary layer physics (X.-M. Hu et al., 2012) or by modifying the urban mixing parameterizations, such as percentage of urban area (PURB) (Wang et al., 2021; Zhang et al., 2021).

Compared to NO₂ and O₃, simulated PM_{2.5} has a lower correlation with EPA AQS station observations, though our model performance is comparable to results reported by many previous studies (e.g., Torres-Vazquez et al., 2022; Wang et al., 2021). Given that SO₂ contributes to secondary PM formation, the relatively poor performance of WRF-CMAQ simulated SO₂ likely influences the PM_{2.5} model-observation agreement. Previous studies have reported that model-station agreement of PM_{2.5} can be strongly influenced by WD, WS, transport, and emissions inventories (Hughes et al., 2021; Zhang et al., 2014) and it is likely that these factors also play a role here. For instance, in the results presented here, we employ MOVES2014a which does not account for emissions from off-network idling of vehicles. MOVES3, released in 2020 (Eyth, 2021), does include these processes, which may be critical for more accurate simulation of PM, particularly in high heavy-duty truck trafficked warehouse environments common within urban settings.

Since the two-way coupled WRF-CMAQ methodology employs nested domains of increasing spatial resolution, we take the opportunity to discuss differences, advantages, and disadvantages of neighborhood-scale (1.3 km) simulations versus those performed at coarser resolutions (4 km). By and large, when model results are assessed against meteorological and pollutant station observations, we find incremental performance improvements at the higher simulation resolution. We do note a few occurrences of slightly degraded model-observation fidelity at higher-resolution (e.g., T2 and O₃), but primarily find that higher resolution simulations marginally improve hindcast simulations of both meteorology and atmospheric chemistry, like previous thematically similar studies (e.g., Torres-Vazquez et al., 2022).

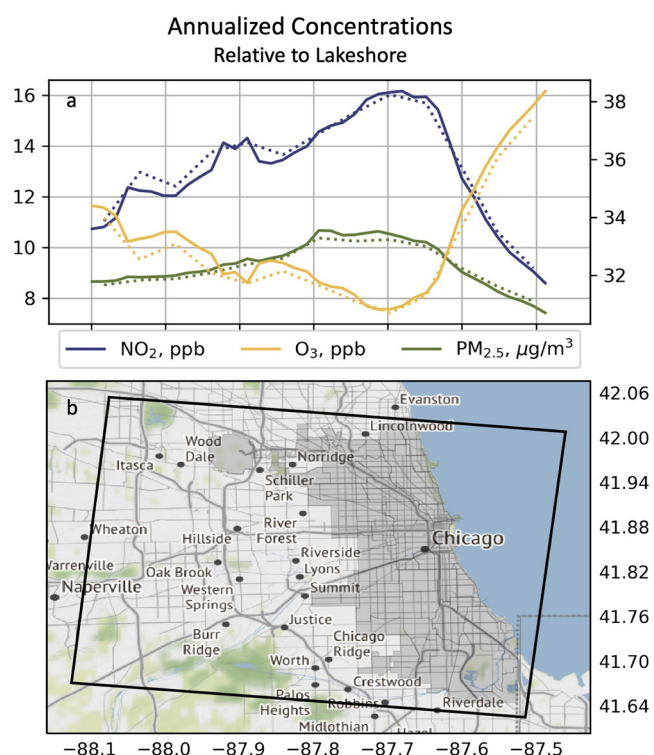


Figure 8. (a) Zonal average of pollutants over Chicago region, from suburbs to city center to lake. Mean pollutant concentrations of NO₂, PM_{2.5}, and O₃ are provided in and (b) the footprint of the averaging domain is depicted around Chicago. Solid line shows the 1.3 km output, while the dotted line shows the 4 km output. Concentrations are plotted across longitudes and stretch from the western suburbs to Lake Michigan in the east.

We note that our 1.3–4 km simulation comparison is not a pure resolution-focused sensitivity experiment. For example, MOVES emissions processing influences on-road sector emissions, and due to differences between the 1.3 and 4 km WRF-simulated meteorology, on road emissions differ over roadways (Figure S6 in Supporting Information S1). However, total emissions are the same within the 1.3 km domain subset of the 4 km domain. Despite emissions differences of 1%–6% over Chicago (Figure S6 in Supporting Information S1), pollutant concentrations differ by only 1%–2% between the 1.3 and 4 km simulations (Figure 6). Ultimately, we find that the most valuable feature of increasing model resolution comes from the finer characterization of emission sources, meteorology, and subsequent pollutant concentrations. To quantitatively demonstrate differences in pollutant gradients between model resolutions, we plot the spatial variogram of the model at EPA AQS observation sites and across random points in the model domain (Figure S11 in Supporting Information S1). We use the methods described in Marzban & Sandgathe, 2009 and Touma et al., 2018, which show that variograms can be used to identify atmospheric features in model simulations and validate model simulations with limited point-observations. Here we use variograms to (a) validate observed spatial pollutant gradients, (b) compare spatial gradients at observation points to simulated pollutants at different model resolutions, and (c) assess differences in simulated spatial variability at different model resolutions. We note that the observation-based variogram is noisy due to the unequal placement of stations over the domain and the low number of stations ($n = 9, 63, 12$ for NO₂, O₃, and PM_{2.5}) relative to the size of the domain ($n = 90,720$) (Figure S10a in Supporting Information S1). At EPA observation sites, we find that the spatial variances of simulated NO₂ and O₃ are closer to observed variances at fine scales (<50 km) in the 1.3 km resolution simulation (Figure S10b in Supporting Information S1). We also compute a “synthetic” variogram (as described in Discussion in Supporting Information S1) computing the variogram at 75 random grid cells across the domain to grid cells within a 50 km radius. We use this analysis to show that

at short distances (<70 km), the 1.3 km simulation has higher pollutant variances across the domain (Figure S10c in Supporting Information S1). As such, we show that at finer spatial scales (Figure 7) and across the domain (<70 km, Figure S11 in Supporting Information S1), the spatial gradients achieved in the 1.3 km output are measurably steeper and have greater fidelity to EPA observations. The ability to resolve air pollution gradients at neighborhood-scale resolutions, using physics- and chemistry-based numerical models, is critical for a number of air quality-relevant disciplines, and continued efforts should be made to both improve model performance and apply these tools to fundamental research queries in the fields of atmospheric chemistry, health, policy, and environmental justice.

4.2. Summary of Chicago Pollutant Findings

Characterizing neighborhood-scale spatial heterogeneities in pollutant concentrations over urban settings, such as Chicago, is critical for better understanding health impacts and constraining the contribution of pollutants to inequitable impacts across population subgroups. In our simulations, we find that Chicago has two to five times higher NO₂ and PM_{2.5} concentrations than neighboring rural areas (Figure 2), and within city limits annualized pollutant concentrations between neighborhoods can vary by a factor of 1.8 (Figure 4). To highlight the utility of high resolution spatially resolved model simulations and intra-city pollutant differences, we analyze zonally averaged annualized pollutant concentrations from Chicago's western suburbs to Lake Michigan in the east (Figure 8). In both 1.3 and 4 km simulations, pollutants over this zonal swath display a distinct west-to-east profile, with NO₂ and PM_{2.5} peaking over the core of the city, and relatively high O₃ concentrations over the lake and in the western suburbs. In general, zonal patterns of O₃ concentrations are the inverse of simulated NO₂ concentrations, which is consistent with the NO_x-saturated regime identified in the core of the city (Figure 7). This inverse pattern is replicated when comparing PM_{2.5} to O₃, albeit with lesser fidelity. In addition to elevated

NO₂ over the city center, a western peak is simulated near O'Hare International Airport (Figure 8a). Despite the inverse NO₂-PM_{2.5}-O₃ zonal pattern, some sections of the city do see relatively high co-occurring concentrations of NO₂, O₃, and PM_{2.5}. For example, Chicago's west side, near -87.8°W, has relatively high concentrations of each pollutant (Figure 8a), likely due to the confluence of highways and industrial areas. The 4 km output shows 0.5 ppb NO₂ and -0.5 ppb lower O₃ in the suburbs (west of -87.8 W), though the 1.3 km simulation shows slightly higher NO₂, O₃, and PM_{2.5} over Chicago. Results such as these suggest that summarizing city-wide air quality using limited observations could be problematic as it does not capture the substantial spatial heterogeneity.

Neighborhood-scale simulations may also prove useful for health, environmental justice, and targeted abatement strategy investigations. Our finding of elevated west side pollutants (Figures 4 and 7) is consistent with previous health-focused work that has identified elevated clusters of air quality related diseases on Chicago's west side (Gupta et al., 2008). Beyond identifying locations of elevated pollutants, high-resolution CTMs may be used to design and test effective mitigation and abatement strategies. For example, given Chicago's current EPA O₃ non-attainment status, designing strategies that effectively target O₃ precursors requires foreknowledge of the City and region's chemical regimes (Figure 7). Simulations capable of characterizing neighborhood-scale O₃ and background VOC:NO_x conditions can provide critical insights into amelioration strategies and can be used to predict and/or avert unintended consequences, such as localized O₃ increases due to NO_x or VOC control measures. High resolution CTMs are particularly suited to this task, given their ability to constrain changes in secondary pollutants, a capability not available in reduced complexity models.

4.3. Limitations

Despite the promising neighborhood-scale results reported here, there are several caveats to bear in mind when considering our two-way coupled WRF-CMAQ results. Chief amongst these considerations is the use of four individual months and their annualized means to characterize the region's air quality and atmospheric chemistry regime. Neighborhood-scale CTM simulations are computationally expensive, which has limited our ability to simulate full seasons or multiple years. Previous studies have demonstrated that internal meteorological variability can have profound consequences on pollutant concentrations (Fiore et al., 2022; Garcia-Menendez et al., 2017), and this facet should be remembered when considering our results. A key example from our study is the high O₃ concentration in our April 2019 simulation. Typically, O₃ in this region peaks in July, however April of 2019 (our chosen simulation month) had higher O₃ concentrations than the typical summer O₃ season. A second key consideration of our study is that the EPA air quality monitoring system was not designed with CTM-validation in mind. AQS sensors are relatively sparse and very often not within urban settings. As such, we use EPA data here, but advocate for the use of hyper-local observing networks to operationally monitor neighborhood-scale air quality and perform model validation.

Further, we note limitations with our model configuration. To perform two-way WRF-CMAQ simulations, we use the default nudging coefficients for the FDDA process above the boundary layer to encourage model-station agreement. This choice has been shown to dampen fine-scale meteorological processes and alter aerosol feedbacks in higher resolution simulations, that is, 4–12 km (Gan et al., 2016; Hogrefe et al., 2015). Future studies should explore the effects of nudging at even finer neighborhood-scale resolutions.

5. Conclusions

In the above, we present the first neighborhood-scale two-way coupled WRF-CMAQ simulations to be performed over a Chicago-centric southern Lake Michigan domain. Both the meteorological and chemical components of our model largely perform at or above recommended standards. We note that our 1.3 km simulation incrementally outperforms our 4 km simulation with respect to most air quality-relevant meteorological variables. In terms of chemical performance, we observe that the 1.3 km simulation outperforms the 4 km simulation with respect to grid cell-to-observation station comparisons for NO₂, O₃, PM_{2.5}, and CO concentrations. SO₂ is the only pollutant that showed higher model-observation fidelity at the coarser model resolution, but this was also the chemical with the lowest model-station agreement at both the 1.3 and 4 km resolutions. Consideration of these performance assessments should be tempered by knowledge that both meteorological and pollutant observing networks allow for model-to-observation comparisons at a maximum of 0.1% of simulated grid cells.

Neighborhood-scale, 1.3 km simulations, are made possible by spatial surrogates curated for the region by LADCO. These surrogates facilitate the simulation of fine-scale features and processes, none more evident than the effect of resolving on-road emissions within urban settings, where we simulate anomalously high roadway-adjacent NO_2 and $\text{PM}_{2.5}$ concentrations, and anomalously low O_3 concentrations. Over our full simulation domain, we find that the highest concentrations of O_3 are found over Lake Michigan during warm season months, where concentrations are simulated to be a full 30% higher than the domain average. In the largest urban area simulated in our domain, Chicago, IL, we find that concentrations of NO_2 are five times higher than the domain average, $\text{PM}_{2.5}$ three times higher, and O_3 slightly lower. We also note spatiotemporal O_3 regime variability within the full model domain, where simulated surface and column average $\text{VOC}:\text{NO}_x$ and $\text{HCHO}:\text{NO}_2$ ratios differ by season and location. Over the full domain, surface conditions are simulated to be NO_x -limited, however over Chicago, conditions are simulated to be transitional—with column average ratios adding further nuance. Likewise over Chicago, our higher resolution simulations show higher average concentrations of NO_2 and $\text{PM}_{2.5}$ than our coarser model simulations, suggesting that coarser models may underestimate exposure to these pollutants and their associated health impacts. Lastly, within Chicago city limits, we find that pollutants can vary by a factor of ~ 2 between neighborhoods, a finding potentially corroborated by observed inequitable health outcomes.

Conflict of Interest

The authors declare no conflicts of interest relevant to this study.

Data Availability Statement

In this study, we use the WRF-CMAQ model (v5.2; Byun & Schere, 2006), which is available from US EPA Office of Research and Development via <https://doi.org/10.5281/zenodo.1079898> (US EPA Office of Research and Development, 2014). The WRFv3.8 model can be downloaded from NCAR: https://www2.mmm.ucar.edu/wrf/users/download/get_source.html (NCAR, 2018). We use the SMOKE 2016 Beta modeling platform (B.H. Baek & Seppanen, 2018) to process the input emissions for WRF-CMAQ which is available here: <http://views.cira.colostate.edu/wiki/wiki/10197> (CIRA, 2019). We use the 4-km spatial surrogates from CMAS (Eyth et al., 2019) which are available with the 2016 Beta Platform (EPA, 2022) and 1.3 km spatial surrogates from LADCO (LADCO, 2022) which are available by request. Due to the large output file sizes and storage (>1 Tb), model output can only be provided by request. For model performance analysis, we use measurements from the National Climate Data Center (NCDC; <https://www.ncei.noaa.gov/data/local-climatological-data/>) (National Climate Dataset, 2022) and the EPA Air Quality System Data Mart (https://aqs.epa.gov/aqsweb/airdata/download_files.html) (EPA Air Quality Datamart, 2022). The data processing and visualization was performed in Python (v3) using the following packages which are available through the Anaconda repository: NetCDF4 (Whitaker et al., 2020), Numpy (Harris et al., 2020), Pandas (Reback et al., 2020), Geopandas (Van den Bossche, Joris, 2022), Cartopy (Elson et al., 2022), Shapely (Gillies, Sean et al., 2022), and Matplotlib (Caswell et al., 2023). The shapefiles for Chicago are available from the Chicago Data Portal via <https://data.cityofchicago.org/> (Chicago Open Data Portal, 2022). The analysis and visualization Python scripts are available on Github the BSD-3-Clause License, available here: <https://doi.org/10.5281/zenodo.7693690>.

Acknowledgments

The authors acknowledge support from the U.S. National Science Foundation Grant CBET-1848683 to DEH; McCormick Center for Engineering Sustainability and Resilience seed grant to DEH; The Ubben Program for Carbon and Climate Science postdoctoral fellowship to JLS; and The Data Science fellowship from the Northwestern Integrated Data-Driven Discovery in Earth and Astrophysical Sciences Program supported by the National Science Foundation DGE-145006 to AM. The authors also extend thanks to three reviewers for substantive feedback on our study and D. Touma for variogram assistance.

References

- Abdi-Oskouei, M., Carmichael, G., Christiansen, M., Ferrada, G., Roozitalab, B., Sobhani, N., et al. (2020). Sensitivity of meteorological skill to selection of WRF-Chem physical parameterizations and impact on ozone prediction during the Lake Michigan ozone study (LMOS). *Journal of Geophysical Research: Atmospheres*, 125(5), e2019JD031971. <https://doi.org/10.1029/2019JD031971>
- Alexeeff, S. E., Roy, A., Shan, J., Liu, X., Messier, K., Apte, J. S., et al. (2018). High-resolution mapping of traffic related air pollution with Google street view cars and incidence of cardiovascular events within neighborhoods in Oakland, CA. *Environmental Health*, 17(1), 38. <https://doi.org/10.1186/s12940-018-0382-1>
- Ashok, A., & Barrett, S. R. H. (2016). Adjoint-based computation of U.S. nationwide ozone exposure isopleths. *Atmospheric Environment*, 133, 68–80. <https://doi.org/10.1016/j.atmosenv.2016.03.025>
- Baek, B. H., & Seppanen, C. (2018). Bokhaeng/Smoke: Smoke V4.5 public release. *Zenodo*. <https://doi.org/10.5281/ZENODO.1321280>
- Bickford, E., Holloway, T., Karambelas, A., Johnston, M., Adams, T., Janssen, M., & Moberg, C. (2014). Emissions and air quality impacts of truck-to-rail freight modal shifts in the Midwestern United States. *Environmental Science & Technology*, 48(1), 446–454. <https://doi.org/10.1021/es4016102>
- Blanchard, C. L., Tanenbaum, S., & Lawson, D. R. (2008). Differences between weekday and weekend air pollutant levels in atlanta; baltimore; chicao; dallas–fort worth; denver; houston; New York; Phoenix; Washington, DC; and surrounding areas. *Journal of the Air & Waste Management Association*, 58(12), 1598–1615. <https://doi.org/10.3155/1047-3289.58.12.1598>

- Byun, D., & Schere, K. L. (2006). Review of the governing equations, computational algorithms, and other components of the models-3 community multiscale air quality (CMAQ) modeling system. *Applied Mechanics Reviews*, 59(2), 51–77. <https://doi.org/10.1115/1.2128636>
- Campbell, P. C., Bash, J. O., & Spero, T. L. (2019). Updates to the Noah land surface model in WRF-CMAQ to improve simulated meteorology, air quality, and deposition. *Journal of Advances in Modeling Earth Systems*, 11(1), 231–256. <https://doi.org/10.1029/2018MS001422>
- Carvalho, D., Rocha, A., Gómez-Gesteira, M., & Santos, C. (2012). A sensitivity study of the WRF model in wind simulation for an area of high wind energy. *Environmental Modelling & Software*, 33, 23–34. <https://doi.org/10.1016/j.envsoft.2012.01.019>
- Caswell, T. A., Lee, A., De Andrade, E. S., Droettboom, M., Hoffmann, T., Klymak, J., et al. (2023). matplotlib/matplotlib: REL: V3.7.0rc1 (Version v3.7.0rc1) [Software]. Zenodo. <https://doi.org/10.5281/ZENODO.592536>
- Chicago Open Data Portal (2022). Community area shapefile [Dataset]. City of Chicago. <https://data.cityofchicago.org/>
- CIRA. (2019). Inventory collaborative 2016beta emissions modeling platform [Dataset]. CIRA. Retrieved from <http://views.cira.colostate.edu/wiki/wiki/10197>
- Clark, L. P., Harris, M. H., Apte, J. S., & Marshall, J. D. (2022). National and intraurban air pollution exposure disparity estimates in the United States: Impact of data-aggregation spatial scale. *Environmental Science and Technology Letters*, 9(9), 786–791. <https://doi.org/10.1021/acs.estlett.2c00403>
- Clough, S. A., Shephard, M. W., Mlawer, E. J., Delamere, J. S., Iacono, M. J., Cady-Pereira, K., et al. (2005). Atmospheric radiative transfer modeling: A summary of the AER codes. *Journal of Quantitative Spectroscopy and Radiative Transfer*, 91(2), 233–244. <https://doi.org/10.1016/j.jqsrt.2004.05.058>
- Dennis, R., Fox, T., Fuentes, M., Gilliland, A., Hanna, S., Hogrefe, C., et al. (2010). A framework for evaluating regional-scale numerical photochemical modeling systems. *Environmental Fluid Mechanics*, 10(4), 471–489. <https://doi.org/10.1007/s10652-009-9163-2>
- Dewitz, J. (2021). National land cover Database (NLCD) 2019 products [Dataset]. U.S. Geological Survey. <https://doi.org/10.5066/P9KZCM54>
- Doak, A. G., Christiansen, M. B., Alwe, H. D., Bertram, T. H., Carmichael, G., Cleary, P., et al. (2021). Characterization of ground-based atmospheric pollution and meteorology sampling stations during the Lake Michigan Ozone Study 2017. *Journal of the Air & Waste Management Association*, 71(7), 866–889. <https://doi.org/10.1080/10962247.2021.1900000>
- Duncan, B. N., Prados, A. I., Lamsal, L. N., Liu, Y., Streets, D. G., Gupta, P., et al. (2014). Satellite data of atmospheric pollution for U.S. air quality applications: Examples of applications, summary of data end-user resources, answers to FAQs, and common mistakes to avoid. *Atmospheric Environment*, 94, 647–662. <https://doi.org/10.1016/j.atmosenv.2014.05.061>
- Dye, T. S., Roberts, P. T., & Korc, M. E. (1995). Observations of transport processes for ozone and ozone precursors during the 1991 Lake Michigan ozone study. *Journal of Applied Meteorology*, 34(8), 1877–1889. [https://doi.org/10.1175/1520-0450\(1995\)034<1877:OOTPFO>2.0.CO;2](https://doi.org/10.1175/1520-0450(1995)034<1877:OOTPFO>2.0.CO;2)
- Elson, P., De Andrade, E. S., Lucas, G., May, R., Hattersley, R., Campbell, E., et al. (2022). SciTools/cartopy: V0.21.1 (version v0.21.1) [Software]. Zenodo. <https://doi.org/10.5281/ZENODO.7430317>
- Emery, C., Liu, Z., Russell, A. G., Odman, M. T., Yarwood, G., & Kumar, N. (2017). Recommendations on statistics and benchmarks to assess photochemical model performance. *Journal of the Air & Waste Management Association*, 67(5), 582–598. <https://doi.org/10.1080/10962247.2016.1265027>
- Emery, C., & Tai, E. (2001). Enhanced meteorological modeling and performance evaluation for two Texas ozone episodes. Final Report Submitted to Texas Natural Resources Conservation Commission, Prepared by ENVIRON. International Corp.
- Emmons, L. K., Schwantes, R. H., Orlando, J. J., Tyndall, G., Kinnison, D., Lamarque, J., et al. (2020). The chemistry mechanism in the community Earth system model version 2 (CESM2). *Journal of Advances in Modeling Earth Systems*, 12(4), e2019MS001882. <https://doi.org/10.1029/2019MS001882>
- EPA. (2018). Review of the primary national ambient air quality standards for oxides of nitrogen. Retrieved from <https://www.govinfo.gov/content/pkg/FR-2018-04-18/pdf/2018-07741.pdf>
- EPA. (2022). Current nonattainment counties for all criteria pollutants. Retrieved from <https://www3.epa.gov/airquality/greenbook/anc1.html>
- EPA Air Quality Datamart. (2022). Hourly criteria pollutants [Dataset]. City of Chicago. Retrieved from <https://data.cityofchicago.org/>
- Eyth, A. (2021). National Emission Inventory (NEI) 2016 modeling platform version 2 [Dataset]. UNC Dataverse. <https://doi.org/10.15139/S3/SAXVSF>
- Eyth, A., Vukovich, J., Farkas, C., & Strum, M. (2019). *Technical support document (TSD): Preparation of emissions inventories for the version 7.2 2016 north American emissions modeling platform*. U.S. Environmental Protection Agency. Retrieved from https://www.epa.gov/sites/default/files/2019-09/documents/2016v7.2_regionalhaze_emismod_tsd_508.pdf
- Fiore, A. M., Hancock, S. E., Lamarque, J.-F., Correa, G. P., Chang, K.-L., Ru, M., et al. (2022). Understanding recent tropospheric ozone trends in the context of large internal variability: A new perspective from chemistry-climate model ensembles. *Environmental Research: Climate*, 1(2), 025008. <https://doi.org/10.1088/2752-5295/ac9cc2>
- Foley, T., Betterton, E. A., Robert Jacko, P. E., & Hillery, J. (2011). Lake Michigan air quality: The 1994–2003 LADCO aircraft Project (LAP). *Atmospheric Environment*, 45(18), 3192–3202. <https://doi.org/10.1016/j.atmosenv.2011.02.033>
- Fountoukis, C., Koraj, D., Denier van der Gon, H. A. C., Charalampidis, P. E., Pilinis, C., & Pandis, S. N. (2013). Impact of grid resolution on the predicted fine PM by a regional 3-D chemical transport model. *Atmospheric Environment*, 68, 24–32. <https://doi.org/10.1016/j.atmosenv.2012.11.008>
- Gan, C.-M., Hogrefe, C., Mathur, R., Pleim, J., Xing, J., Wong, D., et al. (2016). Assessment of the effects of horizontal grid resolution on long-term air quality trends using coupled WRF-CMAQ simulations. *Atmospheric Environment*, 132, 207–216. <https://doi.org/10.1016/j.atmosenv.2016.02.036>
- Garcia-Menendez, F., Monier, E., & Selin, N. E. (2017). The role of natural variability in projections of climate change impacts on U.S. ozone pollution: Natural variability in ozone projections. *Geophysical Research Letters*, 44(6), 2911–2921. <https://doi.org/10.1002/2016GL071565>
- Gillies, S., van der Wel, C., Van den Bossche, J., Taves Mike, W., Arnott, J., Ward, B. C., & Others (2022). Shapely (version 2.0.0). [Software]. Zenodo. <https://doi.org/10.5281/ZENODO.7428463>
- Goldberg, D. L., Anenberg, S. C., Kerr, G. H., Moheg, A., Lu, Z., & Streets, D. G. (2021). TROPOMI NO₂ in the United States: A detailed look at the annual averages, weekly cycles, effects of temperature, and correlation with surface NO₂ concentrations. *Earth's Future*, 9(4), e2020EF001665. <https://doi.org/10.1029/2020EF001665>
- Goldberg, D. L., Loughner, C. P., Tzortziou, M., Stehr, J. W., Pickering, K. E., Marufu, L. T., & Dickerson, R. R. (2014). Higher surface ozone concentrations over the Chesapeake Bay than over the adjacent land: Observations and models from the DISCOVER-AQ and CBODAQ campaigns. *Atmospheric Environment*, 84, 9–19. <https://doi.org/10.1016/j.atmosenv.2013.11.008>
- Goodkind, A. L., Tessum, C. W., Coggins, J. S., Hill, J. D., & Marshall, J. D. (2019). Fine-scale damage estimates of particulate matter air pollution reveal opportunities for location-specific mitigation of emissions. *Proceedings of the National Academy of Sciences of the United States of America*, 116(18), 8775–8780. <https://doi.org/10.1073/pnas.1816102116>

- Gupta, R. S., Zhang, X., Sharp, L. K., Shannon, J. J., & Weiss, K. B. (2008). Geographic variability in childhood asthma prevalence in Chicago. *Journal of Allergy and Clinical Immunology*, 121(3), 639–645. <https://doi.org/10.1016/j.jaci.2007.11.036>
- Harkey, M., Holloway, T., Oberman, J., & Scotty, E. (2015). An evaluation of CMAQ NO₂ using observed chemistry-meteorology correlations: CMAQ evaluation with NO₂-meteorology correlations. *Journal of Geophysical Research: Atmospheres*, 120(22), 11775–11797. <https://doi.org/10.1002/2015JD023316>
- Harris, C. R., Millman, K. J., van der Walt, S. J., Gommers, R., Virtanen, P., Cournapeau, D., et al. (2020). Array programming with NumPy [Software]. *Nature*, 585, 357–362. <https://doi.org/10.1038/s41586-020-2649-2>
- Hogrefe, C., Pouliot, G., Wong, D., Torian, A., Roselle, S., Pleim, J., & Mathur, R. (2015). Annual application and evaluation of the online coupled WRF-CMAQ system over North America under AQMEII phase 2. *Atmospheric Environment*, 115, 683–694. <https://doi.org/10.1016/j.atmosenv.2014.12.034>
- Hu, J., Chen, J., Ying, Q., & Zhang, H. (2016). One-year simulation of ozone and particulate matter in China using WRF/CMAQ modeling system. *Atmospheric Chemistry and Physics*, 16(16), 10333–10350. <https://doi.org/10.5194/acp-16-10333-2016>
- Hu, J., Ostro, B., Zhang, H., Ying, Q., & Kleeman, M. J. (2019). Using chemical transport model predictions to improve exposure assessment of PM_{2.5} constituents. *Environmental Science and Technology Letters*, 6(8), 456–461. <https://doi.org/10.1021/acs.estlett.9b00396>
- Hu, X.-M., Doughty, D. C., Sanchez, K. J., Joseph, E., & Fuentes, J. D. (2012). Ozone variability in the atmospheric boundary layer in Maryland and its implications for vertical transport model. *Atmospheric Environment*, 46, 354–364. <https://doi.org/10.1016/j.atmosenv.2011.09.054>
- Hughes, D. D., Christiansen, M. B., Milani, A., Vermeuel, M. P., Novak, G. A., Alwe, H. D., et al. (2021). PM_{2.5} chemistry, organosulfates, and secondary organic aerosol during the 2017 Lake Michigan Ozone Study. *Atmospheric Environment*, 244, 117939. <https://doi.org/10.1016/j.atmosenv.2020.117939>
- Jbaily, A., Zhou, X., Liu, J., Lee, T.-H., Kamareddine, L., Verguet, S., & Dominici, F. (2022). Air pollution exposure disparities across US population and income groups. *Nature*, 601(7892), 228–233. <https://doi.org/10.1038/s41586-021-04190-y>
- Jiang, X., & Yoo, E. (2018). The importance of spatial resolutions of Community Multiscale Air Quality (CMAQ) models on health impact assessment. *Science of the Total Environment*, 627, 1528–1543. <https://doi.org/10.1016/j.scitotenv.2018.01.228>
- Jin, X., Fiore, A., Boersma, K. F., Smedt, I. D., & Valin, L. (2020). Inferring changes in summertime surface ozone-NO_x-VOC chemistry over U.S. Urban areas from two decades of satellite and ground-based observations. *Environmental Science & Technology*, 54(11), 6518–6529. <https://doi.org/10.1021/acs.est.9b07785>
- Jin, X., Fiore, A. M., Murray, L. T., Valin, L. C., Lamsal, L. N., Duncan, B., et al. (2017). Evaluating a space-based indicator of surface ozone-NO_x-VOC sensitivity over midlatitude source regions and application to decadal trends: Space-based indicator of O₃ sensitivity. *Journal of Geophysical Research: Atmospheres*, 122(19), 10439–10461. <https://doi.org/10.1002/2017JD026720>
- Jing, P., & Goldberg, D. L. (2022). Influence of conducive weather on ozone in the presence of reduced NO_x emissions: A case study in Chicago during the 2020 lockdowns. *Atmospheric Pollution Research*, 13(2), 101313. <https://doi.org/10.1016/j.apr.2021.101313>
- Jing, P., Lu, Z., & Steiner, A. L. (2017). The ozone-climate penalty in the Midwestern U.S. *Atmospheric Environment*, 170, 130–142. <https://doi.org/10.1016/j.atmosenv.2017.09.038>
- Jing, P., Lu, Z., Xing, J., Streets, D. G., Tan, Q., O'Brien, T., & Kambers, J. (2014). Response of the summertime ground-level ozone trend in the Chicago area to emission controls and temperature changes, 2005–2013. *Atmospheric Environment*, 99, 630–640. <https://doi.org/10.1016/j.atmosenv.2014.10.035>
- Kain, J. S. (2004). The Kain-Fritsch convective parameterization: An update. *Journal of Applied Meteorology*, 43(1), 170–181. [https://doi.org/10.1175/1520-0450\(2004\)043<0170:TKCPAU>2.0.CO;2](https://doi.org/10.1175/1520-0450(2004)043<0170:TKCPAU>2.0.CO;2)
- Kleinman, L. I. (1994). Low and high NO_x tropospheric photochemistry. *Journal of Geophysical Research*, 99(D8), 16831. <https://doi.org/10.1029/94JD01028>
- Kopplitz, S., Simon, H., Henderson, B., Liljegren, J., Tonnesen, G., Whitehill, A., & Wells, B. (2022). Changes in ozone chemical sensitivity in the United States from 2007 to 2016. *ACS Environmental Au*, 2(3), 206–222. <https://doi.org/10.1021/acsenvironau.1c00029>
- Kurt, O. K., Zhang, J., & Pinkerton, K. E. (2016). Pulmonary health effects of air pollution. *Current Opinion in Pulmonary Medicine*, 22(2), 138–143. <https://doi.org/10.1097/MCP.0000000000000248>
- LADCO. (2022). Lake Michigan air Directors Consortium (LADCO) technical support document. Retrieved from <https://www.ladco.org/technical/ladco-internal/ladco-projects/ladco-2015-o3-naaqs-moderate-area-sip-technical-support-document/>
- Laughner, J. L., & Cohen, R. C. (2019). Direct observation of changing NO_x lifetime in North American cities. *Science*, 366(6466), 723–727. <https://doi.org/10.1126/science.aax6832>
- Lawal, A. S., Russell, A. G., & Kaiser, J. (2022). Assessment of airport-related emissions and their impact on air quality in Atlanta, GA, using CMAQ and TROPOMI. *Environmental Science & Technology*, 56(1), 98–108. <https://doi.org/10.1021/acs.est.1c03388>
- Liu, X.-H., Zhang, Y., Olsen, K. M., Wang, W.-X., Do, B. A., & Bridgers, G. M. (2010). Responses of future air quality to emission controls over North Carolina, Part I: Model evaluation for current-year simulations. *Atmospheric Environment*, 44(20), 2443–2456. <https://doi.org/10.1016/j.atmosenv.2010.04.002>
- Manson, S., Schroeder, J., Van Riper, D., Kugler, Tracy, & Ruggles, S. (2022). National historical geographic information system: Version 17.0 (version 17.0) [Dataset]. IPUMS. <https://doi.org/10.18128/D050.V17.0>
- Marzban, C., & Sandgathe, S. (2009). Verification with variograms. *Weather and Forecasting*, 24(4), 1102–1120. <https://doi.org/10.1175/2009WAF2222122.1>
- Mesinger, F., DiMego, G., Kalnay, E., Mitchell, K., Shafran, P. C., Ebisuzaki, W., et al. (2006). North American regional reanalysis. *Bulletin of the American Meteorological Society*, 87(3), 343–360. <https://doi.org/10.1175/BAMS-87-3-343>
- Morrison, H., Thompson, G., & Tatarskii, V. (2009). Impact of cloud microphysics on the development of trailing stratiform precipitation in a simulated squall line: Comparison of one-and two-moment schemes. *Monthly Weather Review*, 137(3), 991–1007. <https://doi.org/10.1175/2008mwr2556.1>
- National Climate Dataset. (2022). Local climatological data [Dataset]. NECI. Retrieved from <https://www.ncei.noaa.gov/data/local-climatological-data/>
- NCAR. (2018). WRFv3.8 [Software]. UCAR. Retrieved from https://www2.mmm.ucar.edu/wrf/users/download/get_source.html
- Odman, M. T., White, A. T., Doty, K., McNider, R. T., Pour-Biazar, A., Qin, M., et al. (2019). Examination of nudging schemes in the simulation of meteorology for use in air quality experiments: Application in the Great lakes region. *Journal of Applied Meteorology and Climatology*, 58(11), 2421–2436. <https://doi.org/10.1175/JAMC-D-18-0206.1>
- O'Leary, B. F., & Lemke, L. D. (2014). Modeling spatiotemporal variability of intra-urban air pollutants in Detroit: A pragmatic approach. *Atmospheric Environment*, 94, 417–427. <https://doi.org/10.1016/j.atmosenv.2014.05.010>
- Otte, T. L. (2008). The impact of nudging in the meteorological model for retrospective air quality simulations. Part I: Evaluation against national observation networks. *Journal of Applied Meteorology and Climatology*, 47(7), 1853–1867. <https://doi.org/10.1175/2007JAMC1790.1>

- Pan, S., Choi, Y., Roy, A., & Jeon, W. (2017). Allocating emissions to 4 km and 1 km horizontal spatial resolutions and its impact on simulated NO_x and O₃ in Houston, TX. *Atmospheric Environment*, 164, 398–415. <https://doi.org/10.1016/j.atmosenv.2017.06.026>
- Penn, E., & Holloway, T. (2020). Evaluating current satellite capability to observe diurnal change in nitrogen oxides in preparation for geostationary satellite missions. *Environmental Research Letters*, 15(3), 034038. <https://doi.org/10.1088/1748-9326/ab6b36>
- Pinto, J. P., Lefohn, A. S., & Shadwick, D. S. (2004). Spatial variability of PM 2.5 in urban areas in the United States. *Journal of the Air & Waste Management Association*, 54(4), 440–449. <https://doi.org/10.1080/10473289.2004.10470919>
- Pleim, J. E. (2007). A combined local and nonlocal closure model for the atmospheric boundary layer. Part I: Model description and testing. *Journal of Applied Meteorology and Climatology*, 46(9), 1383–1395. <https://doi.org/10.1175/JAM2539.1>
- Pleim, J. E., & Gilliam, R. (2009). An indirect data assimilation scheme for deep soil temperature in the Pleim–Xiu land surface model. *Journal of Applied Meteorology and Climatology*, 48(7), 1362–1376. <https://doi.org/10.1175/2009JAMC2053.1>
- Pleim, J. E., & Xiu, A. (2003). Development of a land surface model. Part II: Data assimilation. *Journal of Applied Meteorology*, 42(12), 1811–1822. [https://doi.org/10.1175/1520-0450\(2003\)042<1811:DOALSM>2.0.CO;2](https://doi.org/10.1175/1520-0450(2003)042<1811:DOALSM>2.0.CO;2)
- Qin, M., Yu, H., Hu, Y., Russell, A. G., Odman, M. T., Doty, K., et al. (2019). Improving ozone simulations in the Great Lakes Region: The role of emissions, chemistry, and dry deposition. *Atmospheric Environment*, 202, 167–179. <https://doi.org/10.1016/j.atmosenv.2019.01.025>
- Reback, J., McKinney, W., Jbrockmendl, Bossche, J. V. D., Augspurger, T., Cloud, P., et al. (2020). pandas-dev/pandas: Pandas 1.0.3 (Version v1.0.3) [Software]. Zenodo. <https://doi.org/10.5281/ZENODO.3715232>
- Rethinking the Ozone Problem in Urban and Regional Air Pollution. (1991). *Rethinking the ozone problem in urban and regional air pollution* (p. 1889). National Academies Press. <https://doi.org/10.17226/1889>
- Schnell, J. L., & Prather, M. J. (2017). Co-occurrence of extremes in surface ozone, particulate matter, and temperature over eastern North America. *Proceedings of the National Academy of Sciences*, 114(11), 2854–2859. <https://doi.org/10.1073/pnas.1614453114>
- Schroeder, J. R., Crawford, J. H., Fried, A., Walega, J., Weinheimer, A., Wisthaler, A., et al. (2017). New insights into the column CH₂ O/NO₂ ratio as an indicator of near-surface ozone sensitivity: CH₂ O/NO₂ as indicator of O₃ sensitivity. *Journal of Geophysical Research: Atmospheres*, 122(16), 8885–8907. <https://doi.org/10.1002/2017JD026781>
- Seinfeld, J. H., & Pandis, S. N. (2016). *Atmospheric chemistry and physics: From air pollution to climate change* (3rd ed.). John Wiley & Sons.
- Sharma, S., Sharma, P., & Khare, M. (2017). Photo-chemical transport modelling of tropospheric ozone: A review. *Atmospheric Environment*, 159, 34–54. <https://doi.org/10.1016/j.atmosenv.2017.03.047>
- Sillman, S., Logan, J. A., & Wofsy, S. C. (1990). The sensitivity of ozone to nitrogen oxides and hydrocarbons in regional ozone episodes. *Journal of Geophysical Research*, 95(D2), 1837. <https://doi.org/10.1029/JD095iD02p01837>
- Simon, H., Baker, K. R., & Phillips, S. (2012). Compilation and interpretation of photochemical model performance statistics published between 2006 and 2012. *Atmospheric Environment*, 61, 124–139. <https://doi.org/10.1016/j.atmosenv.2012.07.012>
- Skamarock, W., Klemp, J., Dudhia, J., Gill, D., Barker, D., Wang, W., et al. (2008). *A Description of the advanced research WRF version 3 [Application/pdf]* (p. 1002 KB). UCAR/NCAR. <https://doi.org/10.5065/D68S4MVB>
- SMOKE v4.5 User's Manual. (2017). *SMOKE v4.5 User's Manual*. The Institute for the Environment - The University of North Carolina at Chapel Hill. Retrieved from https://www.cmascenter.org/smoke/documentation/4.5/manual_smokev45.pdf
- Southerland, V. A., Anenberg, S. C., Harris, M., Apte, J., Hystad, P., van Donkelaar, A., et al. (2021). Assessing the distribution of air pollution health risks within cities: A neighborhood-scale analysis leveraging high-resolution data sets in the Bay area, California. *Environmental Health Perspectives*, 129(3), 037006. <https://doi.org/10.1289/EHP7679>
- Tai, A. P. K., Mickley, L. J., & Jacob, D. J. (2010). Correlations between fine particulate matter (PM_{2.5}) and meteorological variables in the United States: Implications for the sensitivity of PM_{2.5} to climate change. *Atmospheric Environment*, 44(32), 3976–3984. <https://doi.org/10.1016/j.atmosenv.2010.06.060>
- Tessum, C. W., Paolella, D. A., Chambliss, S. E., Apte, J. S., Hill, J. D., & Marshall, J. D. (2021). PM 2.5 pollutants disproportionately and systemically affect people of color in the United States. *Science Advances*, 7(18), eabf4491. <https://doi.org/10.1126/sciadv.abf4491>
- The CESM2 Development Team. (2019). CESM2.1/CAM-chem instantaneous output for boundary conditions [Dataset]. UCAR/NCAR - Atmospheric Chemistry Observations and Modeling Laboratory. <https://doi.org/10.5065/NMP7-EP60>
- Thompson, T. M., Saari, R. K., & Selin, N. E. (2014). Air quality resolution for health impact assessment: Influence of regional characteristics. *Atmospheric Chemistry and Physics*, 14(2), 969–978. <https://doi.org/10.5194/acp-14-969-2014>
- Torres-Vazquez, A., Pleim, J., Gilliam, R., & Pouliot, G. (2022). Performance evaluation of the meteorology and air quality conditions from multi-scale WRF-CMAQ simulations for the long Island sound tropospheric ozone study (LISTOS). *Journal of Geophysical Research: Atmospheres*, 127(5), e2021JD035890. <https://doi.org/10.1029/2021JD035890>
- Touma, D., Michalak, A. M., Swain, D. L., & Diffenbaugh, N. S. (2018). Characterizing the spatial scales of extreme daily precipitation in the United States. *Journal of Climate*, 31(19), 8023–8037. <https://doi.org/10.1175/JCLI-D-18-0019.1>
- Tran, T., Tran, H., Mansfield, M., Lyman, S., & Crosman, E. (2018). Four dimensional data assimilation (FDDA) impacts on WRF performance in simulating inversion layer structure and distributions of CMAQ-simulated winter ozone concentrations in Uintah Basin. *Atmospheric Environment*, 177, 75–92. <https://doi.org/10.1016/j.atmosenv.2018.01.012>
- Travis, K. R., Jacob, D. J., Fisher, J. A., Kim, P. S., Marais, E. A., Zhu, L., et al. (2016). Why do models overestimate surface ozone in the Southeast United States? *Atmospheric Chemistry and Physics*, 16(21), 13561–13577. <https://doi.org/10.5194/acp-16-13561-2016>
- US EPA Office Of Research And Development. (2014). Cmaq v5.0.2. Zenodo. <https://doi.org/10.5281/ZENODO.1079898>
- Van den Bossche, Joris (2022). GeoPandas: Easy, fast and scalable geospatial analysis in Python [Software]. Zenodo. <https://doi.org/10.5281/ZENODO.7320003>
- Wang, J., Xue, P., Pringle, W., Yang, Z., & Qian, Y. (2022). Impacts of Lake surface temperature on the summer climate over the Great lakes region. *Journal of Geophysical Research: Atmospheres*, 127(11), e2021JD036231. <https://doi.org/10.1029/2021JD036231>
- Wang, K., Tong, Y., Gao, J., Zhang, X., Zuo, P., Wang, C., et al. (2021). Pinpointing optimized air quality model performance over the Beijing-Tianjin-Hebei region: Mosaic approach. *Atmospheric Pollution Research*, 12(11), 101207. <https://doi.org/10.1016/j.apr.2021.101207>
- Wang, K., Zhang, Y., Yu, S., Wong, D. C., Pleim, J., Mathur, R., et al. (2021). A comparative study of two-way and offline coupled WRF v3.4 and CMAQ v5.0.2 over the contiguous US: Performance evaluation and impacts of chemistry–meteorology feedbacks on air quality. *Geoscientific Model Development*, 14(11), 7189–7221. <https://doi.org/10.5194/gmd-14-7189-2021>
- Whitaker, J., Khrulev, C., Huard, D., Paulik, C., Hoyer, S., Filipe, et al. (2020). Unidata/netcdf4-python: Version 1.5.5 release (version v1.5.5rel2) [Software]. Zenodo. <https://doi.org/10.5281/ZENODO.4308773>
- Wong, D. C., Pleim, J., Mathur, R., Binkowski, F., Otte, T., Gilliam, R., et al. (2012). WRF-CMAQ two-way coupled system with aerosol feedback: Software development and preliminary results. *Geoscientific Model Development*, 5(2), 299–312. <https://doi.org/10.5194/gmd-5-299-2012>
- Xiu, A., & Pleim, J. E. (2001). Development of a land surface model. Part I: Application in a mesoscale meteorological model. *Journal of Applied Meteorology*, 40(2), 192–209. [https://doi.org/10.1175/1520-0450\(2001\)040<0192:DOALSM>2.0.CO;2](https://doi.org/10.1175/1520-0450(2001)040<0192:DOALSM>2.0.CO;2)

- Zhang, H., Chen, G., Hu, J., Chen, S.-H., Wiedinmyer, C., Kleeman, M., & Ying, Q. (2014). Evaluation of a seven-year air quality simulation using the Weather Research and Forecasting (WRF)/Community Multiscale Air Quality (CMAQ) models in the eastern United States. *Science of the Total Environment*, 473–474, 275–285. <https://doi.org/10.1016/j.scitotenv.2013.11.121>
- Zhao, Y., Zhang, L., Zhou, M., Chen, D., Lu, X., Tao, W., et al. (2019). Influences of planetary boundary layer mixing parameterization on summertime surface ozone concentration and dry deposition over North China. *Atmospheric Environment*, 218, 116950. <https://doi.org/10.1016/j.atmosenv.2019.116950>